European Journal of Pharmacology 1008 (2025) 178317

Contents lists available at ScienceDirect

European Journal of Pharmacology

journal homepage: www.elsevier.com/locate/ejphar

# Ellagic acid-loaded nanovesicles rescue LTP impairment and neuroinflammation in an AD *ex-vivo* model

Nunzia Maisto [a], Sepideh Dashtiani [a,b], Jacopo Forte [c,d], Maria Grazia Ammendolia [e], Viviana Triaca [f], Federica Rinaldi [d,1], Dalila Mango [a,*,1]

[a] School of Pharmacy, Department of Biology, University of Rome 'Tor Vergata', Via della Ricerca Scientifica, Rome, 00133, Italy
[b] Department of Physiology and Pharmacology "V. Erspamer", Sapienza University of Rome, P.le Aldo Moro 5, Rome, 00185, Italy
[c] Department of Basic Biotechnological Sciences, Intensivological and Perioperative Clinics, Catholic University of Sacred Heart, Largo Francesco Vito 1, 00168, Rome, Italy
[d] Department of Drug Chemistry and Technology, Sapienza University of Rome, P.le Aldo Moro 5, Rome, 00185, Italy
[e] National Center for Innovative Technologies in Public Health, Istituto Superiore di Sanità (ISS), Viale Regina Elena 299, Rome, 00161, Italy
[f] Institute of Biochemistry and Cell Biology, National Research Council (CNR), International Campus A. Buzzati-Traverso, Rome, Italy

ARTICLE INFO

*Keywords:*
Amyloid beta
Ellagic acid
Drug delivery systems
Microglia
Neuroinflammation
Synaptic plasticity

ABSTRACT

Neurodegenerative diseases, such as Alzheimer's disease (AD), cause progressive neurological decline and major healthcare challenges. AD is marked by deterioration in learning, memory, and cognition, leading to dementia. Early-stage AD brains show accumulation of amyloid-beta (Aβ) protofibrils and plaques, particularly in the hippocampus, associated with chronic neuroinflammation and impaired synaptic plasticity that drive cognitive decline. Current AD treatments primarily relieve symptoms without slowing disease progression, and existing monoclonal antibodies targeting Aβ plaques have controversial side effects. This has driven interest in natural compounds like polyphenols for their broad biological activities.

Ellagic acid (EA), a natural polyphenol, exhibits antioxidant, anti-inflammatory, and neuroprotective properties. Experimental models of neurodegenerative diseases have shown EA's potential to improve memory and cognition by modulating synaptic plasticity. This study has evaluated EA's impact on hippocampal synaptic plasticity and its neuroprotective effects against $A\beta_{1-42}$-mediated impairments using electrophysiological recordings and immunofluorescence analysis, evaluating microglial morphological normalization as well as interleukins expression. It has been found that, in *ex vivo* brain slices, EA modulated synaptic plasticity at high concentration, while at the dose that *per se* does not alter neurotransmission it rescued LTP and basal neurotransmission impairment $A\beta_{1-42}$ mediated, and normalized neuroinflammation by reducing interleukins expression released by activated microglia. However, EA's poor water solubility and extensive first-pass metabolism limit its clinical use. Here, EA has been encapsulated in non-ionic surfactant vesicles (NSVs), and the formulation (EA-NSVs) has demonstrated a neuroprotective effect at a lower dose compared to free EA, effectively rescuing synaptic impairment induced by $A\beta_{1-42}$.

## 1. Introduction

In the field of neuropharmacology, new treatments are urgently needed as neurodegenerative diseases, including Alzheimer's disease (AD), are characterized by progressive neurological decline, posing significant challenges to healthcare systems (Yap et al., 2019). Notably, AD, the most prevalent neurodegenerative disorder (Jha et al., 2018; Li et al., 2025), is characterized by a progressive decline in neurological functions and is associated with a gradual deterioration of learning, memory, and cognitive functions, ultimately leading to dementia (Nisticò et al., 2012). The predominant hypothesis explaining neurodegeneration in AD, which is also based on presymptomatic and early human post-mortem human brain, is the "amyloid cascade hypothesis," which posits that the accumulation and aggregation of amyloid-beta (Aβ) protofibrils and plaques in various brain regions, especially the hippocampus, induce chronic neuroinflammation, resulting in neuronal

* Corresponding author.
*E-mail address:* dalila.mango@uniroma2.it (D. Mango).
[1] These authors contributed equally to this work.

https://doi.org/10.1016/j.ejphar.2025.178317
Received 29 July 2025; Received in revised form 28 October 2025; Accepted 31 October 2025
Available online 1 November 2025

death and loss of synaptic and neuronal functions (Haass and Selkoe, 2022; Mecca et al., 2022). Currently, treatment options for AD are limited, with most therapies only alleviating symptoms without modifying the disease course, or with monoclonal antibodies targeting Aβ plaques and characterized by different side effects. Consequently, research efforts are increasingly focused on developing new candidate drugs, and natural substances, like polyphenol compounds, have attracted considerable interest due to their pleiotropic activities (Khan et al., 2020; Zhu et al., 2023).

In this context, Ellagic Acid (EA), a polyphenolic compound abundant in fruits and nuts, has emerged as a promising candidate due to its anti-inflammatory and neuroprotective properties (Ahmed et al., 2016; Atta-Ur-Rahman et al., 2001; Kiasalari et al., 2017; Sanadgol et al., 2017), as it has demonstrated the ability to improve learning and memory deficits, reduce Aβ aggregation, and mitigate tau hyperphosphorylation (Dionísio et al., 2015; Javaid et al., 2021; Kiasalari et al., 2017; Li et al., 2025). Specifically, EA decreases the expression of inflammatory cytokines, including IL-1β and IL-6 (Farbood et al., 2015), which are directly involved in the alteration of synaptic plasticity mechanisms (Goshen et al., 2007; Tancredi et al., 2000) that underlie the cognitive decline characteristic of AD (Mecca et al., 2022; Rowan et al., 2003; Shankar et al., 2008; Terry et al., 1991). Also, it can mitigate hippocampal oxidative stress and neuroinflammation by stimulating IGF-1 signalling (Chen et al., 2024), and reverse alterations in the expression of α-amino-3-hydroxy-5-methyl-4-isoxazolepropionic acid (AMPA) receptors and their scaffolding proteins in the cerebral cortex, leading to improvements in memory and cognitive functions (Singh and Prasad, 2024). However, there is no evidence of the EA's functional rescue properties in the AD context, and this study has been evaluated its impact on hippocampal synaptic plasticity and its neuroprotective effects against $A\beta_{1\text{-}42}$-mediated impairments and neuroinflammation.

Despite the promising results, the therapeutic potential of EA is limited by its poor water solubility and extensive first-pass metabolism, resulting in low bioavailability (Murugan et al., 2009). A valid approach to get over this limit is represented by delivering EA in drug delivery systems (Li et al., 2023), as non-ionic surfactant vesicles (NSVs), also known as niosomes. These are colloidal systems able to encapsulate, protect, and deliver both hydrophilic and lipophilic compounds (Bhardwaj et al., 2020). Very similar to liposomes, their structure, consisting of surfactant components, makes them more stable than phospholipids-based nanocarriers (Bartelds et al., 2018), and a versatile drug delivery system adaptable to different kinds of administration routes (Bhardwaj et al., 2020; Marianecci et al., 2016). For instance, it is an innovative and useful strategy especially in the neuropharmacology field (Khalin et al., 2014; Zheng et al., 2024), where brain drug delivery is characterized by important limitations due to the presence of the Blood Brain Barrier (Abbott et al., 2010). One of the most promising strategies is to combine this nanocarrier with intranasal delivery, with the condition that the drug delivery systems must meet stringent physicochemical requirements, particularly with respect to particle size (Adnet et al., 2020; Migliore et al., 2010). Indeed, an optimal particle size is crucial to potentially ensure effective transport across the nasal mucosa and to reach the brain via the olfactory and trigeminal pathways (Adnet et al., 2020; Migliore et al., 2010).

Thereby, in this study after evaluating the effects of free EA on synaptic plasticity and neuroinflammation, EA was loaded into NSVs (EA-NSVs), formulated and characterized to be potentially administered by Nose to Brain delivery (Huang et al., 2024; Rinaldi et al., 2019). Finally, EA-NSVs' activity has been also evaluated *ex vivo* on hippocampal synaptic plasticity and the neuroprotective effects against $A\beta_{1\text{-}42}$-mediated impairments were assessed in in the same model in comparision with free EA.

## 2. Material and methods

### 2.1. Animals

All animals were handled in compliance with the national (D.Lgs 26/2014) and international guidelines for animal welfare (European Communities Council Directive, 2010/64/EU). All efforts were made to minimize the number of animals used and their suffering. C57/Bl6J mice were housed at the EBRI Rita Levi-Montalcini Foundation (Rome, Italy).

### 2.2. Materials

Ellagic acid (EA) was bought by CARLO ERBA Reagents S.r.l. (Milan, Italy). Picrotoxin was purchased from Abcam (Milan, Italy). $A\beta_{1\text{–}42}$ and $A\beta_{42\text{-}1}$ were purchased from GenScript (USA). For the electrophysiological recordings drugs were dissolved in DMSO and the final concentration of DMSO did not exceed 0.5 %. For immunofluorescence, goat anti-Iba1 (AB5076) was purchased from Abcam, while rabbit anti-IL-6-(Invitrogen 701028), rabbit anti-IL-1B (Invitrogen MA5-47038), and all the Alexa Fluor® from Invitrogen by Thermofisher. Pluronic F-127, Sorbitan trioleate (Span 85), Cholesterol (Chol), Diphenylhexatriene (DPH), Ethanol (EtOH), Pyrene, Sodium 2-(4-(2-hydroxyethyl) piperazine-1-yl (Hepes), Ethanol F.U., Methanol, Chloroform and DMSO were bought from Sigma-Aldrich (Milan, Italy).

### 2.3. Electrophysiological recordings

#### 2.3.1. Slice preparation and ex vivo drug treatments

Parasagittal hippocampal slices (250–350 μm thick) from C57BL6/J mice (30–40 days old male and female) were obtained as described (Maisto et al., 2023; Piccioni et al., 2024). Particularly, were cut with a vibratome (VT 1200S, Leica) in cold (0 °C) artificial cerebrospinal fluid (aCSF) saturated with 95 % $O_2$, 5 % $CO_2$ (pH 7.4; Cold Spring Harbor Protocols) and left to recover for 1 h in aCSF at room temperature (RT) (Maisto et al., 2023). Before extracellular recordings, slices were incubated in saturated aCSF for 30 min with $A\beta_{1\text{-}42}$ (200 nM) at RT, while in whole-cell patch clamp experiments, $A\beta_{1\text{-}42}$ (500 nM) was perfused for 10 min during recordings (Mango et al., 2016; Piccioni et al., 2024). As a control, $A\beta_{42\text{-}1}$ was applied for the same time and concentration as $A\beta_{1\text{-}42}$ at RT. In the EA group, the slices were incubated in aCSF with EA (3–100 μM) for 30 min alone or with $A\beta_{1\text{-}42}$ (200 nM) at RT. Also, in the EA-NSVs group, the slices were incubated with EA-NSVs (3–10 μM) for 30 min alone or with $A\beta1\text{-}_{42}$ (200 nM) at RT.

#### 2.3.2. Extracellular field recordings

Extracellular field recordings were performed in CA1-CA3 region of the hippocampus. Field excitatory postsynaptic potential (fEPSP) was elicited with a stimulating electrode placed in the *stratum radiatum* close to the Schaffer collateral pathway and recorded with a glass electrode placed in CA1. The paired-pulse ratio (PPR) was assessed at interstimulus intervals from 50 to 500 ms and was calculated as the ratio of the second fEPSP amplitude/first fEPSP amplitude. Before the Long-Term Potentiation (LTP) induction, a baseline was recorded for 20 min. The LTP protocol was characterized by a theta-burst stimulation protocol consisting of four pulses at 100 Hz, with the bursts repeated at 5 Hz, and each tetanus including three 10-burst trains separated by 15 s (Maisto et al., 2023; Piccioni et al., 2024). Responses were recorded for 60 min after tetanization and measured as fEPSP amplitude normalized on the baseline. All measurements results are reported as a percentage of the ratio of fEPSP, measured at each time point, and the mean of fEPSP baseline recorded in the first 20 min. For statistical comparisons, the "n" indicates the number of brain slices.

#### 2.3.3. Whole-cell voltage-clamp recordings

Whole-cell voltage-clamp recordings were carried out from hippocampal pyramidal neurons. The spontaneous excitatory postsynaptic

currents (sEPSC) were isolated using picrotoxin in the perfusion medium to block GABAA receptors. For paired-pulse (PP) experiments, paired-pulse stimuli (50 ms inter-pulse interval) were elicited with a stimulating electrode placed in the stratum radiatum of CA1. PPR was evaluated as the ratio of the second EPSC amplitude to the first EPSC amplitude. α-amino-3-hydroxy-5-methyl-4-isoxazolepropionic acid/N-methyl-D-aspartate (AMPA/NMDA) ratio was performed considering the ratio of the peak amplitude of EPSC, holding the cell at −80 mV (AMPA component), on the peak amplitude of EPSC at +40 mV holding potential (NMDA component) in a 2 ms window at 60 ms delay from the stimulation artifact according to previous published (De Jaco et al., 2017). For statistical comparisons, the "n" indicates the number of neurons.

### 2.4. Immunofluorescence staining

After *ex vivo* pharmacological treatments (Section 2.3.1), parasagittal hippocampal slices were fixed in 4 % paraformaldehyde (PFA) overnight at 4 °C. The following day, slices were washed in 0.1 M phosphate-buffered saline (PBS) in a separate 24-well plate at RT. Slices were then prepared for immunofluorescence by permeabilization with 0.3 % Triton X-100 and blocking with 10 % of normal donkey serum for 1h at RT. Slices where then incubate with $NH_4Cl$ (50mM) for 30 min at RT for autofluorescence blocking. For single labeling, slices were incubated overnight at 4 °C with a goat anti-Iba1 primary antibody (1:1000 in PBS), followed by 1.30-h incubation at RT with an Alexa Fluor 647-conjugated anti-goat secondary antibody (1:1000 in PBS). For double labeling, slices were incubated with a combination of rabbit anti-IL-6 or anti-IL-1β (1:100 in PBS) and goat anti-Iba1 (1:1000 in PBS) primary antibodies overnight at 4 °C. The next day, after washing in PBS they were incubated in PBS with a combination of Alexa Fluor 488-conjugated anti-rabbit (1:1000) and Alexa Fluor 647-conjugated anti-goat (1:1000) secondary antibodies at RT for 1.30h. Finally, slices were incubated in PBS with DAPI (1:1000, 15') at RT, mounted in anatomical order with ProLong Diamond Antifade Mountant (P36931; Life Technologies, Carlsbad, CA, USA) onto SuperFrost Plus glass slides, and cover-slipped using #1 thickness (0.13–0.16 mm) glass coverslips (Fisher).

#### 2.4.1. Imaging acquisition and analysis

Brain slice imaging was performed using a Leica SP5 laser-scanning confocal microscope with a 40 × oil immersion objective (NA = 1.25). An ultraviolet diode laser (405 nm), an argon laser (488 nm), and a helium-neon (HeNe) laser (633 nm) were used as excitation sources. Images were acquired at a resolution of 1024 × 1024 pixels per frame, with 18–20 frames per z-stack taken at 1.00 μm intervals, using Leica FAV software.

Image analysis acquisition was carried out in FIJI (ImageJ, NIH) and the maximum intensity projections were generated from z-stacks using the Z-project function for further analysis. Morphological analysis was performed to measure area, perimeter, and circularity index of Iba1-positive microglial cells, using a Fiji plugin designed for semi-automated segmentation, tracking, and 2D morphometric analysis of microglial cells (Martinez et al., 2023). All images were analysed by setting the following parameters: intensity threshold: 1.50 (relative); minimum object size: 100 $\mu m^2$; maximum cell skeleton length: 450 μm; maximum contact length: 20 μm. Further, by the same original binary masks, Sholl analysis was conducted to quantify the number of intersections at different radius through the "Neuroanatomy" Fiji plugin (Arshadi et al., 2021). In both cases for the statistical analysis, the "n" used represents the number of microglial cells.

Whereas, to assess interleukins expression and localization, images, relative to interleukins expression, were manually thresholded and binarized using the Otsu method. Area and perimeter were then measured for each field of view (FOV), as acquired with a 40× oil-immersion objective, using the "Analyze Particles" tool, with the following setting: particle size set from 10 $\mu m^2$ to infinity, and circularity ranging from 0.01 to 1.00 values. All measurements were normalized and expressed as percentage of the vehicle-treated control group. In this case for the statistical analysis, the "n" represents the FOV, thereby the brain slices; when the expression was analysed within the $Iba1^+$ cells, the "n" represents the interleukins expression within the microglial cells.

### 2.5. Preparation of empty and loaded niosomes (NSVs)

Empty NSVs have been prepared and characterized in a previous work (Maisto et al., 2023). Loaded niosomes (EA-NSVs, Table 1) were prepared by the same thin film layer preparation technique followed by extrusion, as described in the previous paper (Maisto et al., 2023). Surfactants and/or lipophilic components (DPH/EA) were solubilized in the organic solvent which was evaporated using the rotary evaporator. The dried films were hydrated by Hepes buffer (0.01 M, pH 7.4), and the obtained dispersion was vortexed and then a microtip-sonication (Vibracell-VCX 500, Sonics, Taunton, MA, USA; amplitude 20 %, temperature 25 °C, 2 min) was employed to obtain unilamellar vesicles (Giuli et al., 2024). Subsequently, the vesicles were extruded at RT by a Lipex ExtruderTM (Vancouver, Canada) equipped with polycarbonate membrane filters extruding the suspensions for 2 cycles through cellulose filters (Millex1 Syringe Filters, Millipore) of 1.2 μm pore size.

### 2.6. Physicochemical characterization of EA loaded niosomes

#### 2.6.1. Dynamic Light Scattering measurements

Dynamic Light Scattering (DLS, Malvern Zetasizer Nano ZS90, Malvern Instruments Ltd., Worcestershire, United Kingdom) was utilized to characterize EA-NSVs and NSVs, assessing their hydrodynamic diameter and ζ-potential. The results, expressed as means, include the hydrodynamic diameter (nm) and ζ-potential (mV) of the surfactant vesicles. The polydispersity index (PDI) was also determined to measure the size distribution breadth; a PDI value below 0.3 indicates a homogeneous and monodisperse population. For statistical analysis, the "n" represents the mean value from three different samples per group.

#### 2.6.2. Physiochemical stability over time and in biological fluids

The vesicular formulations were stored at 4 °C or 25 °C for 45 days to evaluate their physical stability, with periodic assessments of hydrodynamic diameter and ζ-potential. Aliquots from each batch were taken at specified intervals (1, 15, 30, and 45 days) and analysed using the DLS instrument.

Additionally, the physicochemical stability of the vesicular formulations was tested in biological fluids, such as the aCSF (pH 7.4; Cold Spring Harbor Protocols) (Maisto et al., 2023) or the Simulated Nasal fluid (SNF) (2.192 g NaCl, 0.145 g CaCl2 and 0.745 g KCl in 250 mL) containing mucin (0.1 %, w/v). Each sample was incubated in aCSF and SNF separately. In particular, 0.55 mL of the sample (55 %) was added to 0.45 mL of aCSF or SNF containing mucin (0.1 % w/w) (45 %) and put into a test tube to mimic the physiological condition. The magnetic stirring was applied, and the temperature was maintained at 37 °C when in the presence of aCSF (Anderson et al., 2003), and 34 °C with SNF containing mucin (0.1 % w/w) (Corsaro et al., 2022). The mean hydrodynamic diameter and ζ-potential of the nanoparticle suspensions were measured by DLS after 1, 2, and 3 h, from three different samples per group.

**Table 1**
Sample composition.

| Sample | Span 85 (mM) | F-127 (mM) | Chol (mM) | EA (mg/mL) |
|---|---|---|---|---|
| EA-NSVs | 10 | 5 | 15 | 2 |

*2.6.2.1. Transmission electron microscopy (TEM).* The formation of loaded EA-NSVs vesicles, as well as their morphological aspects in the biological fluids, was evaluated by using transmission electron microscopy. Samples dispersed in Hepes buffer, aCSF (pH 7.4, Cold Spring Harbor Protocols) (Maisto et al., 2023) and SNF containing mucin (0.1 %, w/v), were drop-cast onto a formwar carbon-coated grid and stained with a 1 % aqueous solution of phosphotungstic acid (PTA) adjusted at pH 7.0. After air drying, the negatively stained samples were imaged at an accelerating voltage of 100 kV using a FEI 280S transmission electron microscope (FEI Company, Hillsboro, OR, USA). To optimize image editing, Adobe Photoshop CS4 software (Adobe Systems, San Jose, CA, USA) was used.

*2.6.3. Bilayer characterization*

Fluorometric analysis was conducted to characterize vesicular bilayer fluidity using DPH, a lipophilic fluorescent probe (as described in section 2.4), to evaluate the anisotropy value, which is inversely proportional to membrane rigidity (Lentz, 1989). DPH fluorescent measurements were performed using a luminescence spectrometer (LS5013, PerkinElmer, Waltham, MA, USA) at RT. The excitation and emission wavelengths were 400 and 425 nm, respectively, and the fluorescence anisotropy (r) was calculated using Equation (1):

$$\text{Fluorescence anisotropy (r)} = \frac{(Ivv \times Ivh) \times G}{(Ivv + 2Ivh) \times G} \quad (1)$$

where $I_{vv}$, $I_{vh}$, $I_{hv}$, and $I_{hh}$ are fluorescent intensities, subscript v (vertical) and h (horizontal) represent the orientation of polarized light, and $G = I_{hv}/I_{hh}$ factor is the ratio of sensitivity of the detection system for vertically and horizontally polarized light. Results are presented as the mean value from three different samples.

### 2.7. Determination of drug entrapment and in vitro drug release

*2.7.1. Determination of drug entrapment efficiency (E.E.%)*

The concentration of EA in loaded EA-NSVs was measured by UV–visible spectroscopy (Lambda 25, PerkinElmer, Waltham, MA, USA) equipped with a 1.0 cm path-length quartz cell. The absorbance of EA at $\lambda = 255$ nm has been measured by diluting EA-NSVs in Ethanol: Hepes 70:30 (vol: vol), with empty NSVs diluted in Ethanol: Hepes 70:30 as reference. The E.E. % was calculated by the ratio between the amount of EA entrapped in the NSVs and the amount of EA added to niosomes during the preparation procedure, by the following equation (2).

$$\text{E.E. \%} = \frac{Entrapped\ drug\ (mg)}{Entrapped\ drug\ (mg)} \times 100 \quad (2)$$

The results are shown as the average of three different batches.

To evaluate the stability in terms of decomposition/degradation of EA, EA-NSVs loaded were analysed by UV–vis analysis over time at definite time intervals (1, 15, 30 and 45 days), and at two different storage temperatures, 4 °C and RT. For statistical analysis, the "n" indicates the mean value from three different sample.

*2.7.2. In vitro drug release profile*

*In vitro* drug release experiments were carried out by putting the loaded EA-NSVs in a dialysis bag (molecular weight cut-off: 8000 by Spectra/Por®). The dialysis bag was immersed in the release medium pH 7.3 at 37 °C and gently magnetically stirred during the experiment, composed by Ethanol (70 %) given the lipophilic EA nature, and Hepes Buffer 10 mM, pH 7.4 or aCSF (30 %). The EA concentration in the acceptor medium, composed of EtOH:Hepes (70:30) or EtOH:aCSF (70:30), was detected at different time points (0, 1, 2, 3, 4, 5, 6, 7, 8 and 24h) by ultraviolet (UV) spectrophotometer, with the same settings described in section 2.7.1. To perform quantification analysis, 1 mL of external medium was withdrawn, immediately analysed, and then re-inserted back. The % of released EA was calculated considering the ratio between the absorbance detected at a specific time point over the absorbance maximum of the samples, and both measures were made at the same dilution. Particularly, the absorbance maximum was measured by causing the disruption of the vesicular bilayer with methanol. The data collected represent the mean values over three repeated independent experiments, and errors are reported as SD.

### 2.8. Statistics

For electrophysiology and immunofluorescence experiments, data were expressed as mean ± S.E.M., and the statistical significance was evaluated by Student's t-test (paired or unpaired data) for comparisons between two groups, or with one-way ANOVA by Bonferroni's or Tukey's post hoc test for comparisons across groups. Statistical significance was set starting from $p < 0.05$. In LTP experiments significance was evaluated considering the mean of LTP magnitude of the last 10 min between groups. Changes in amplitude or frequency of sEPSC were compared according to their mean value using the Student's t-test. For all statistical comparisons, the "n" used was the number of brain slices or cells. For immunofluorescence analysis, the statistical comparison has been made considering the mean value of the different groups and running one-way ANOVA.

One-way ANOVA was carried out for the statistical analysis of EA-NSVs characterization studies. Multiple comparisons were performed according to Tukey's test for ζ -potential, hydrodynamic diameter, and polydispersity index (PDI), respectively. A p-value <0.05 was considered statistically significant.

## 3. Results

### 3.1. High concentration of Ellagic acid modulates synaptic plasticity in hippocampal slices

To evaluate any potential effect of EA on hippocampal synaptic plasticity and transmission, *ex vivo* hippocampal slices were pre-incubated for 30 min with EA diluted at different EA concentrations according to studies present in the literature (Feng et al., 2009). Electrophysiological measures were performed recording a stable baseline and after 20 min a theta-burst protocol to Schaffer collaterals was delivered to induce Long Term Potentiation (LTP). In slices incubated with the highest concentration of EA (100 μM), we found an increase in LTP magnitude compared to the vehicle, suggesting a concentration-dependent response (Fig. 1A, B). Indeed, EA at the concentration from 3 to 30 μM, did not affect LTP magnitude (EA 3 μM, 149.0 ± 7.61, n = 5, vs vehicle 149.52 ± 6.21, n = 6, $p > 0.05$; EA 10 μM 147.79 ± 9.28 n = 5, vs vehicle 149.52 ± 6.21, n = 5, $p > 0.05$; EA 30 μM 150.86 ± 7.11 n = 5, vs vehicle 149.52 ± 6.21, n = 5, $p > 0.05$; Fig. 1A and B), while treatment with EA 100 μM was able to increase significantly LTP compared to vehicle (EA 100 μM 169.90 ± 8.50, n = 5, vs vehicle 149.52 ± 6.21, n = 5 $p < 0.001$; Fig. 1A and B). Whereas, in slices treated with EA (3–100 μM) for 30 min, neither change in PPR was observed compared to vehicle slices. Data indicated that at all inter-pulse intervals, PPR was indistinguishable between EA groups and vehicles ($p > 0.05$; for each experimental group n = 5; Fig. 1C). These data suggest that, while any synaptic changes are mediated at lower concentration without effect *per se* on basal neurotransmission, at higher concentration EA can affect long-term synaptic plasticity.

### 3.2. Ellagic acid reverses $A\beta_{1\text{-}42}$-mediated LTP impairment in hippocampal slices

To investigate a potential neuroprotective effect of EA, the same concentrations used in the first characterization by extracellular field recordings have been tested against $A\beta_{1\text{-}42}$ alterations in *ex vivo* model. In previous studies, it was shown that Aβ oligomers perturb hippocampal synapses (Chapman et al., 1999; Chen et al., 2000; Varga et al.,

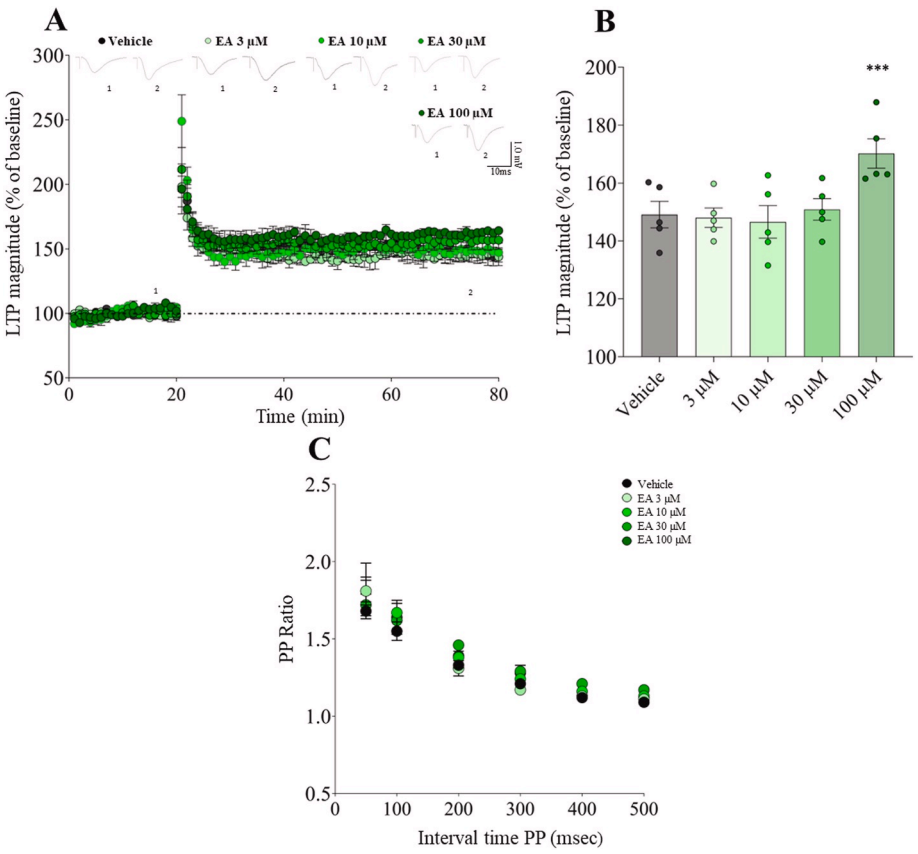


**Fig. 1. Ellagic acid (EA) modulates long-term potentiation (LTP) in the hippocampus**. Data are presented as mean value ± SEM. ***p < 0.001 vs vehicle. (A) Above representative traces for the vehicle in each experimental condition of EA (3, 10, 30 and 100 μM) are shown; below summary graph of the averaged time course of LTP induced by theta-burst stimulation. (B) Histograms illustrate the magnitude of LTP (% of baseline) in each experimental condition. Dots represent the mean of last 10 min of LTP recorded for each brain slice. (C) PPR is induced by pairs of stimulation delivered at several interstimulus intervals (20, 50, 100, 200, 300, 500 ms).

2015), affecting synaptic plasticity and neurotransmission in *ex vivo* model (Mango et al., 2016; Piccioni et al., 2021). In this context, in our experimental condition, we confirmed that *ex vivo* hippocampal slices incubated with $A\beta_{1\text{-}42}$ (200 nM) for 30 min, were characterized by a significative reduction of LTP magnitude (vehicle 155.92 ± 4.90, vs $A\beta_{1\text{-}42}$ 130.48 ± 2.55, for each n = 8, $p < 0.001$; Fig. 2), and in that concern it was evaluated the neuroprotective effect of EA co-incubated with $A\beta_{1\text{-}42}$, against the LTP impairment induced by $A\beta_{1\text{-}42}$. Results showed that EA was able to restore the LTP magnitude in the range of concentration 10–100 μM, but not at low concentration of 3 μM (EA 3 μM + $A\beta_{1\text{-}42}$ 133.11 ± 1.60, n = 5, vs $A\beta_{1\text{-}42}$ 130.48 ± 2.55, n = 8; $p > 0.05$; Fig. 2A and B). Notably, the LTP restoring effect was evident at 10 μM of EA (EA 10 μM + $A\beta_{1\text{-}42}$ 140.11 ± 3.26, n = 6, vs $A\beta_{1\text{-}42}$ 130.48 ± 2.55, n = 8, $p < 0.05$, Fig. 2C and D), and the effect was more noticeable at 30 μM (EA 30 μM + $A\beta_{1\text{-}42}$ 145.59 ± 5.48, n = 6, vs $A\beta_{1\text{-}42}$ 130.48 ± 2.55, n = 8; $p < 0.001$; Fig. 2E and F), while the efficacy remained constantly at 100 μM representing a pharmacological plateau (EA 100 μM + $A\beta_{1\text{-}42}$ 147.30 ± 5.11, n = 6, vs $A\beta_{1\text{-}42}$ 130.48 ± 2.55, n = 8; , $p < 0.001$; Fig. 2G and H).

### 3.3. EA normalizes $A\beta_{1\text{-}42}$-mediated changes in synaptic neurotransmission

To assess the neuroprotective activity of EA against $A\beta_{1\text{-}42}$-mediated changes at the synaptic level, we performed experiments in whole-cell patch clamp configuration from CA1 pyramidal neurons, using the lower concentrations (3 and 10 μM) which don't alter *per se* the synaptic transmission and synaptic plasticity in the control condition. As described previously (Mango et al., 2016), $A\beta_{1\text{-}42}$ influences the basal synaptic transmission when applied in perfusion (10 min) at 500 nM, determining significant alterations in excitatory neurotransmission and receptor function (Mango et al., 2016). To evaluate the neuroprotective effect of EA, it has been analysed the PPR, the AMPA/NMDA ratio, and the spontaneous excitatory neurotransmission (sEPSC), analysing both amplitude and frequency.

According to the literature (Mango et al., 2016; Monfort and Felipo, 2010; Piccioni et al., 2024; Puzzo et al., 2005), $A\beta_{1\text{-}42}$ affects PPR inducing an increase of this parameter correlated with a reduction in the neurotransmitter release (Vehicle 1.99 ± 0.55, n = 9, vs + $A\beta_{1\text{-}42}$ 2.87 ± 0.69, n = 9, $p < 0.01$; Fig. 3A). In this context, pre-incubation with EA at 3 μM (30 min) was not able to prevent the PPR alteration due to $A\beta_{1\text{-}42}$ perfusion (EA 3 μM, 1.92 ± 0.85, n = 5, vs + $A\beta_{1\text{-}42}$, 2.94 ± 1.20, n = 5, $p < 0.01$; Fig. 3A), and it didn't affect the pre-synaptic changes either (Vehicle 1.99 ± 0.55, n = 9, vs EA 3 μM, 1.92 ± 0.85, n = 5, $p > 0.05$; Fig. 3A), according also to LTP experiments. Conversely, treatment with EA 10 μM has shown the ability to forestall the change induced by $A\beta_{1\text{-}42}$ (EA 10 μM 2.40 ± 1.30, n = 5, vs + $A\beta_{1\text{-}42}$ 2.44 ± 1.32, n = 5, $p > 0.05$; Fig. 3A).

Furthermore, it has been investigated the AMPA/NMDA ratio, an index of AMPA and NMDA receptor presence at the post-synaptic level which is know to be affected by $A\beta_{1\text{-}42}$ (Mango et al., 2016). Application of $A\beta_{1\text{-}42}$ induced an increase in AMPA/NMDA ratio compared to the vehicle (Vehicle 1.23 ± 0.62, n = 5, vs + $A\beta_{1\text{-}42}$, 1.98 ± 0.51, n = 5, $p < 0.01$; Fig. 3B), which means a reduction of AMPA and NMDA currents at post-synaptic levels, mediated by receptor internalization fostered by $A\beta_{1\text{-}42}$ (Shankar et al., 2008; Snyder et al., 2005). This effect is prevented by pre-treatment with EA at 10 μM (EA 10 μM 1.42 ± 1.30, n = 5, vs + $A\beta_{1\text{-}42}$ 1.58 ± 1.26, n = 5, $p > 0.05$; Fig. 3B) but not with EA 3 μM

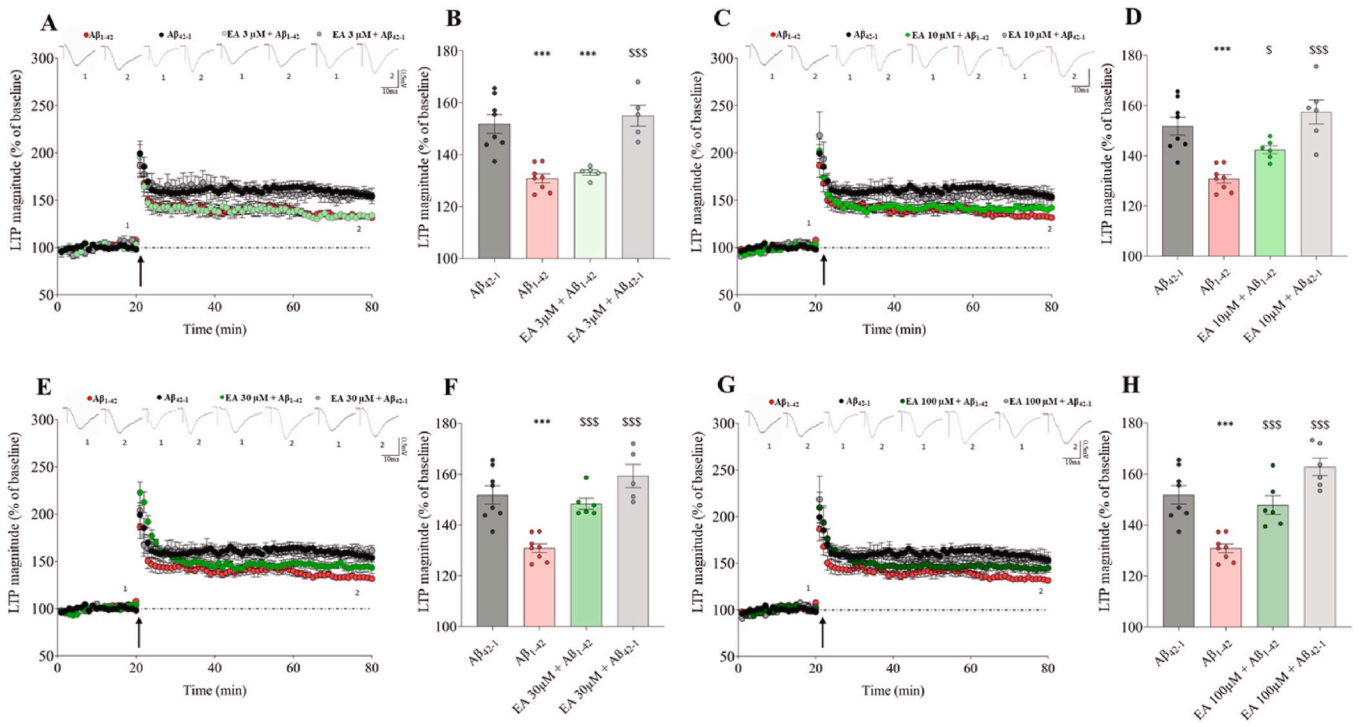


**Fig. 2. EA reverses Aβ$_{1-42}$-mediated LTP impairment.** Statistic symbol: ***p < 0.001 vs Aβ$_{42-1}$, $p < 0.05 vs Aβ$_{1-42}$, $$$p < 0.001 vs Aβ$_{1-42}$. Data are presented as percentage of fEPSP mean value normalized on the fEPSP mean of baseline ± SEM. (A), (C), (E), (G) Above representative traces for slices in respective experimental group: Aβ$_{1-42}$, Aβ$_{42-1}$, EA (at different concentration) + Aβ$_{1-42}$ and EA (at different concentration) + Aβ$_{42-1}$; below summary graph of the averaged time course of LTP. (B), (D), (F), (H) Histograms illustrating the magnitude of LTP (% of baseline). Dots represent the mean of last 10 min of LTP recorded for each brain slice.

pre-treatment (EA 3 μM 1.21 ± 0.83, n = 5, vs + Aβ$_{1-42}$, 2.21 ± 1.25, n = 5, p < 0.01; Fig. 3B). Finally, the rescue of Aβ-mediated effects by EA was also analysed in terms of spontaneous excitatory transmission recording (sEPSC) from CA1 pyramidal neurons, considering the parameters of amplitude and frequency (Mango et al., 2016). The ability of Aβ$_{1-42}$ to suppress both sEPSC amplitude and frequency compared to the vehicle (amplitude: Vehicle, 100.00 ± 9.36, n = 5, vs + Aβ$_{1-42}$ 83.24 ± 5.70, n = 5, p < 0.05; frequency: Vehicle 100.00 ± 7.00, n = 5, vs + Aβ$_{1-42}$ 54.46 ± 5.84, n = 5, p < 0.01; Fig. 3C and D) was hampered by pre-treatment with EA at 10 μM (amplitude: EA 10 μM 100.00 ± 8.17, n = 5, vs + Aβ$_{1-42}$ 72.24 ± 10.90, n = 5, p > 0.05; frequency: EA 10 μM, 100.00 ± 2.81, n = 5, vs + Aβ$_{1-42}$, 102.6 ± 5.67, n = 5, p > 0.05; Fig. 3C and D), but not at the concentration of 3 μM (amplitude: EA 3 μM 100.00 ± 2.29, n = 5, vs + Aβ$_{1-42}$ 74.40 ± 8.09, n = 5, p < 0.01; frequency: EA 3 μM 100.00 ± 3.99, n = 5, vs + Aβ$_{1-42}$, 87.28 ± 3.33, n = 5, p < 0.05; Fig. 3C and D).

All these results indicate that EA (10 μM) has a neuroprotective effect against alterations induced by Aβ$_{1-42}$ on both synaptic neurotransmission and plasticity.

### 3.4. *Morphological evidence of microglial normalization in Ellagic Acid–Mediated neuroinflammation attenuation from Aβ$_{1-42}$ ex vivo application*

Previously, we have demonstrated that in our *ex vivo* experimental conditions, Aβ$_{1-42}$ treatment induces a neuroinflammation response in microglia with metabolic and morphological shift (Piccioni et al., 2024). To assess the effect of EA in modulating neuroinflammation in our *ex vivo* system, it has been evaluated the microglial activation analysing Iba1$^+$ microglial morphology in the CA1 region of hippocampal slices incubated *ex vivo* with Aβ$_{1-42}$. According to electrophysiological results, EA was only tested at 10 μM, a concentration shown to preserve basal synaptic transmission and plasticity in our *ex vivo* model without *per se* neuroactive effects.

Microglial morphology is a sensitive readout of functional state, shifting from a highly ramified, surveillant profile under physiological conditions to a hypertrophic and amoeboid form during neuroinflammatory responses (Godeanu and Cătălin, 2025; Harry and Kraft, 2008; Reddaway et al., 2023; Sierra et al., 2024; Vidal-Itriago et al., 2022). In our analysis focusing on the total cell footprint, Aβ$_{1-42}$ exposure induced a significant increase in microglial cell body size, as reflected by increased area (Vehicle 102.50 ± 5.47, n = 88, vs Aβ$_{1-42}$ 122.23 ± 4.91, n = 108, p < 0.01; Fig. 4C) and perimeter per Iba1$^+$ cell (Vehicle 98.86 ± 3.87, n = 88, vs Aβ$_{1-42}$ 124.54 ± 5.05, n = 108, p < 0.001; Fig. 4D), indicating a pro-inflammatory phenotype. Concomitantly, the circularity index (CI), a morphological parameter used as a proxy for microglial activation and structural remodelling during neuroinflammatory responses (Young and Morrison, 2018), reflects process complexity and somatic shape, which was significantly reduced in Aβ$_{1-42}$-treated slices (Vehicle 0.30 ± 1.15, n = 25, vs Aβ$_{1-42}$ 0.34 ± 0.91, n = 58, p < 0.01; Fig. 4E). EA completely normalized these changes, restoring area (EA + Aβ$_{1-42}$ 90.04 ± 3.91, n = 50, vs Aβ$_{1-42}$ 122.23 ± 3.57, n = 58, p < 0.05; Fig. 4C), perimeter (EA + Aβ$_{1-42}$ 88.97 ± 3.70, n = 50, vs Aβ$_{1-42}$ 124.81 ± 2.65, n = 58, p < 0.01; Fig. 4D), and CI (EA + Aβ$_{1-42}$ 0.39 ± 0.01, n = 50, vs Aβ$_{1-42}$ Aβ$_{1-42}$ 0.34 ± 0.91, n = 58, p < 0.05; Fig. 4E).

To further quantify microglial structural complexity, Sholl analysis was performed to capture the extent and distribution of branching as a function of radial distance from the soma. Aβ$_{1-42}$ significantly reduced the number of intersections across radii, with a lower peak value compared to the treatment with EA (EA + Aβ$_{1-42}$ 6.14 ± 0.31, n = 59, vs Aβ$_{1-42}$ 4.8 ± 0.43, n = 79, p < 0.05; Fig. 4F). The radius at which the maximum branching occurred was also shifted inward following Aβ$_{1-42}$ co-treatment (EA + Aβ$_{1-42}$ 33.30 ± 1.02 μm, n = 104, vs Aβ$_{1-42}$ 26.50 ± 0.87 μm, n = 115, p < 0.01; Fig. 4F), indicating process retraction and restore of this spatial ramification by EA. Additional morphometric parameters confirmed this trend: branchiness, representing process density (Martinez et al., 2023; Young and Morrison, 2018), was reduced

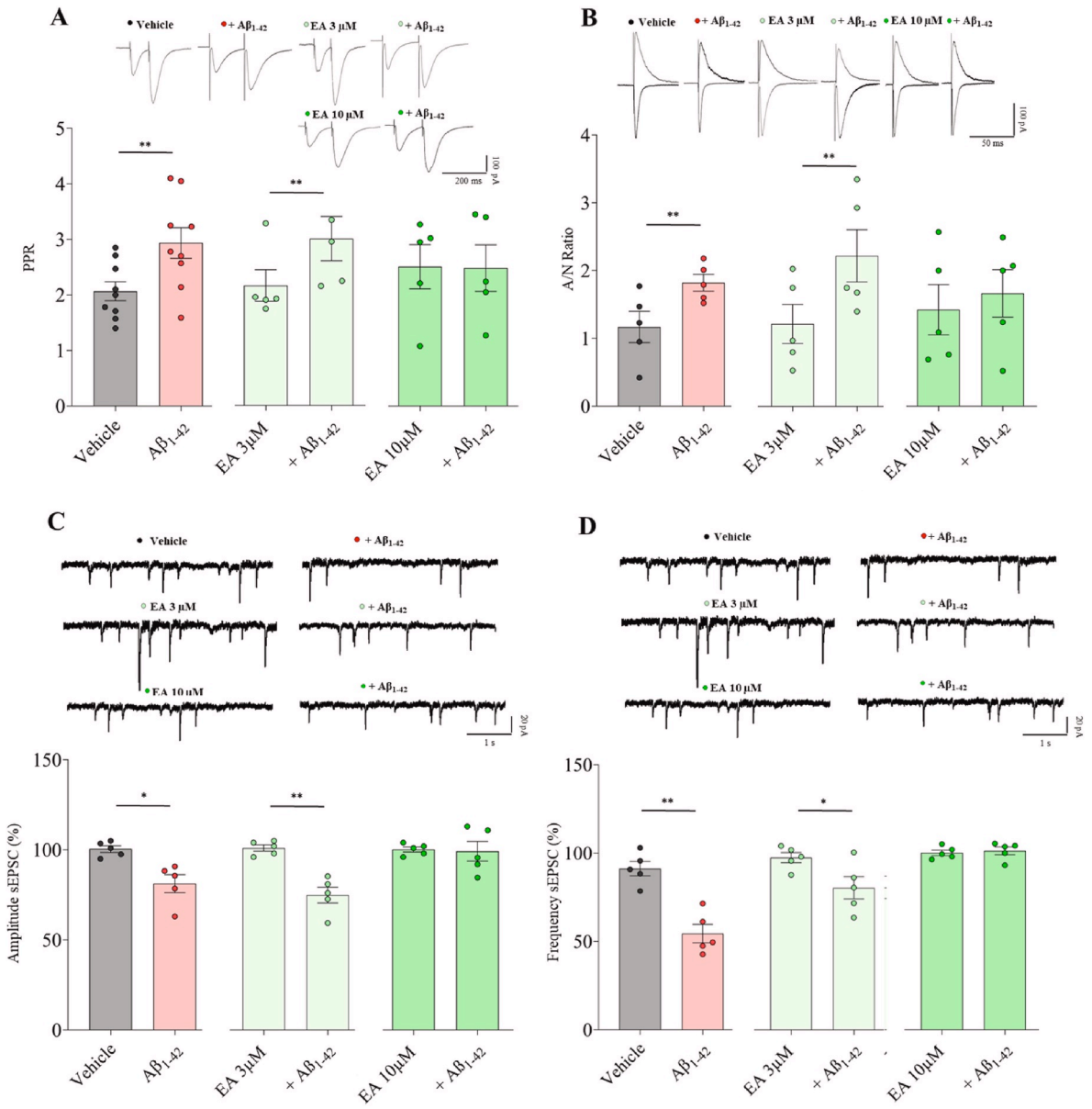


**Fig. 3. EA normalizes *ex vivo* $A\beta_{1-42}$-mediated change in PP transmission, AMPA/NMDA ratio, and excitatory neurotransmission at 10 μM.** Statistic symbol: *p < 0.05, **p < 0.01. Data are presented as mean value ± SEM. (A) Representative traces (top) and corresponding histograms (bottom) showing changes in paired-pulse ratio (PPR) across experimental conditions. (B) Above representative traces from different experimental conditions are shown; below histograms show the AMPA/NMDA ratio in each experimental condition. (D) Representative traces for each group (top) and histograms (bottom) displaying the effects on sEPSC amplitude and frequency (expressed as % of baseline). Each dot represents the value from an individual neuron.

by $A\beta_{1-42}$ and rescued by EA (EA + $A\beta_{1-42}$ 0.070 ± 0.004, n = 104, vs $A\beta_{1-42}$ 0.085 ± 0.003, n = 115, $p < 0.05$; Fig. 4G), while straightness, reflecting directional elongation (Martinez et al., 2023; Young and Morrison, 2018), was significantly increased with EA (EA + $A\beta_{1-42}$ 1.98 ± 0.06, n = 104, vs $A\beta_{1-42}$ 1.36 ± 0.07, n = 115, $p < 0.01$; Fig. 4H). These metrics together reinforce the interpretation that EA prevents the Aβ-induced morphological shift toward a less ramified phenotype.

Collectively, these results highlight that EA at 10 μM maintains microglial morphological complexity and prevents inflammatory remodelling induced by $A\beta_{1-42}$, underscoring its potential as a modulator of neuroinflammation in early pathological conditions.

### 3.5. *Ellagic acid mitigates $A\beta_{1-42}$-mediated neuroinflammation by reducing IL-6 and IL-1β levels through microglial activation*

To investigate the anti-inflammatory effects of EA on $A\beta_{1-42}$-induced neuroinflammation, we analysed also the expression and spatial distribution of pro-inflammatory cytokines, IL-6 and IL-1β, in $Iba1^+$ microglial cells within the hippocampal CA1 region using immunofluorescence analysis. IL-6 and IL-1β are key mediators of neuroinflammation, known to be upregulated in activated microglia during Alzheimer's disease pathology and they are also linked to promote synaptic dysfunction and neuronal damage (Goshen et al., 2007; Tancredi et al., 2000).

We quantified both vesicular and puncta-like, considering respectively diffuse/clustered integrated density (InDen) of both IL-6 and IL-1β positive regions per FOV, and within microglial regions of interest (ROIs) taken by the binary mask created using the morphological plugin (Martinez et al., 2023), as described in the previous section. We interpret the puncta density as likely reflects early or regulated cytokine processing and trafficking, whereas the larger IL-6-positive area indicates more advanced or pathological cytokine accumulation (Saed et al.,

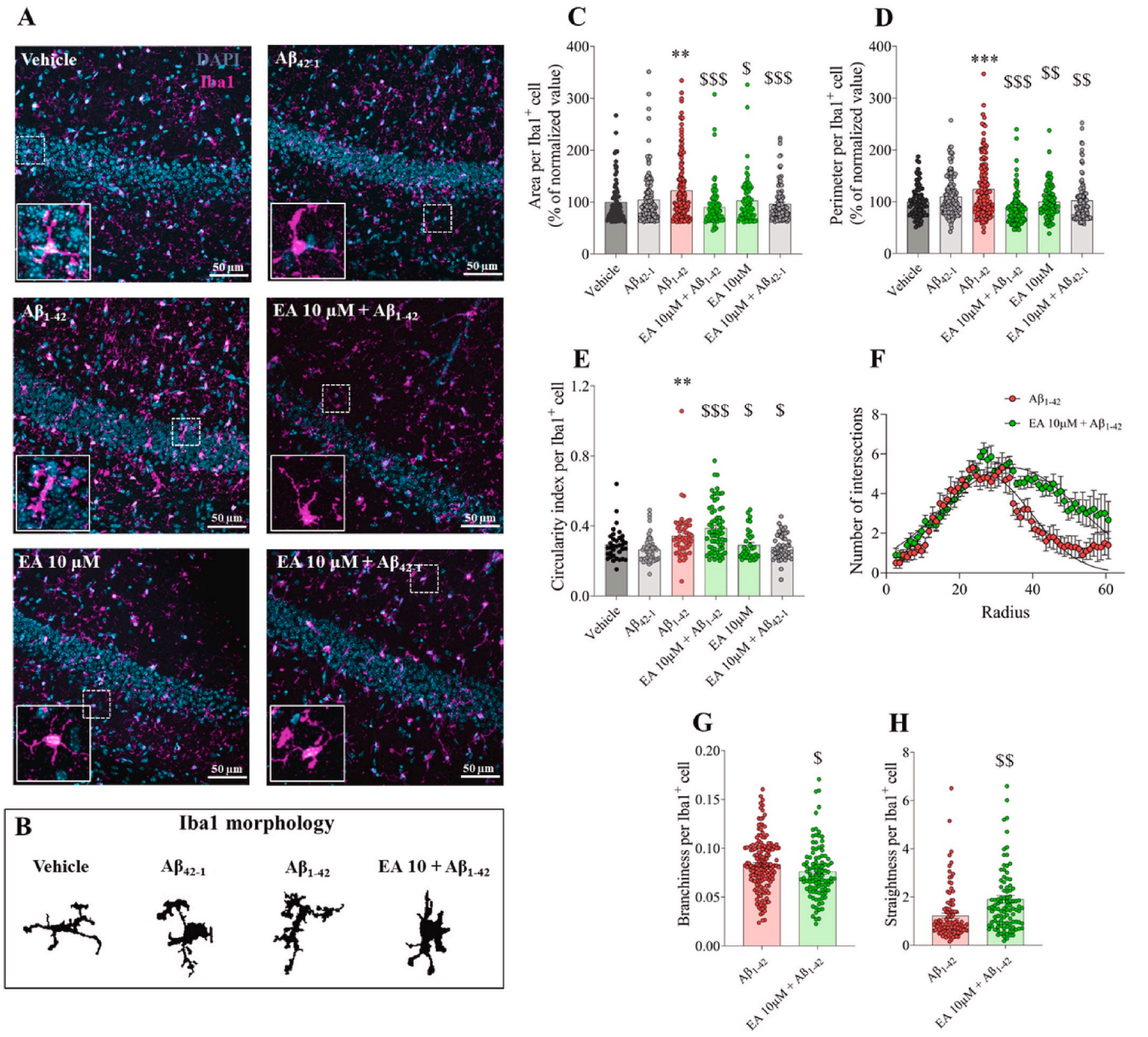


**Fig. 4. Ellagic acid preserves microglial morphology and complexity in *ex vivo* Aβ$_{1-42}$ treated hippocampal slice.** Statistic symbols: **p < 0.01, ***p < 0.001 vs Vehicle; $p < 0.05, $$p < 0.01, $$$p < 0.00 vs Aβ$_{1-42}$. Data are presented as mean value ± SEM. (A) Representative confocal images (40x) of Iba1 immunostaining in the CA1 region of hippocampal slices across different *ex vivo* pharmacological treatment groups. Microglia (magenta: Iba1$^{+}$) and nuclei (cyan: DAPI) are shown. Insects display higher magnification of individual microglial cells. (B) Binary masks of representative microglial cells used for morphometric analysis. (C–E) Quantification of cell (C) area, (D) perimeter, (E) circularity. Each dot represents a microglial cell. (F) Sholl analysis showing the number of intersections as a function of radius from the soma. Each dot represents the mean of the number of intersections across microglial cells at the same radius. (G, H) Quantification of branching parameters: straightness and branchiness. Each dot represents the value of microglial cell. (For interpretation of the references to colour in this figure legend, the reader is referred to the Web version of this article.)

2024). Indeed, application of Aβ$_{1-42}$ markedly increased IL-6 expression per FOV, as shown by a significant rise in area and integrated density compared to vehicle-treated slices (area: vehicle 100.96 ± 1.92, n = 6, vs Aβ$_{1-42}$ 143.12 ± 3.12, n = 6, p < 0.001; IntDen: vehicle 102.17 ± 2.87, n = 6, vs Aβ$_{1-42}$ 148.31 ± 3.55, n = 6, p < 0.001 Fig. 5B and C). Importantly, EA pre-treatment significantly reduced both the total IL-6 area and IntDen per FOV (area: EA + Aβ$_{1-42}$ 101.02 ± 1.47, n = 6, vs Aβ$_{1-42}$ 143.12 ± 3.12, n = 6, p < 0.001; IntDen: EA + Aβ$_{1-42}$ 98.45 ± 2.08, n = 6, vs Aβ$_{1-42}$ 143.75 ± 3.11, n = 6, p < 0.001; Fig. 5B and C). This attitude has been found also analysing the IL-1β expression which in EA + Aβ$_{1-42}$ treatment was significantly lower than Aβ$_{1-42}$ alone (area: EA + Aβ$_{1-42}$ 99.94 ± 10.21, n = 5, vs Aβ$_{1-42}$ 136.55 ± 5.62, n = 5, p < 0.001; IntDen: EA + Aβ$_{1-42}$ 98.05 ± 5.41, n = 5, vs Aβ$_{1-42}$ 136.55 ± 5.62, n = 5, n = 6, p < 0.001; Fig. 5B1 and C1).

Similarly, at the microglial cellular level, the expression area and intensity of IL-6 within Iba1$^{+}$ cells was also markedly elevated by Aβ$_{1-42}$ (area: vehicle 99.80 ± 10.45, n = 22, vs Aβ$_{1-42}$ 154.15 ± 15.14 n = 37, p < 0.001; IntDen: vehicle 100.00 ± 2.92, n = 22, vs Aβ$_{1-42}$: 173.90 ± 6.19, n = 37, p < 0.001; 5D and E), which was significantly reversed by EA (area: EA + Aβ$_{1-42}$ 74.89 ± 15.31, n = 19, vs Aβ$_{1-42}$: 154.15 ± 15.14 n = 37, p < 0.01; IntDen: EA + Aβ$_{1-42}$ 116.40 ± 5.31, n = 19, vs Aβ$_{1-42}$: 173.90 ± 6.19, n = 37, p < 0.05; Fig. 5D and E). A similar pattern in the overall expression and within microglia cells, was observed also for IL-1β, where treatment with Aβ$_{1-42}$ significantly increases the number and

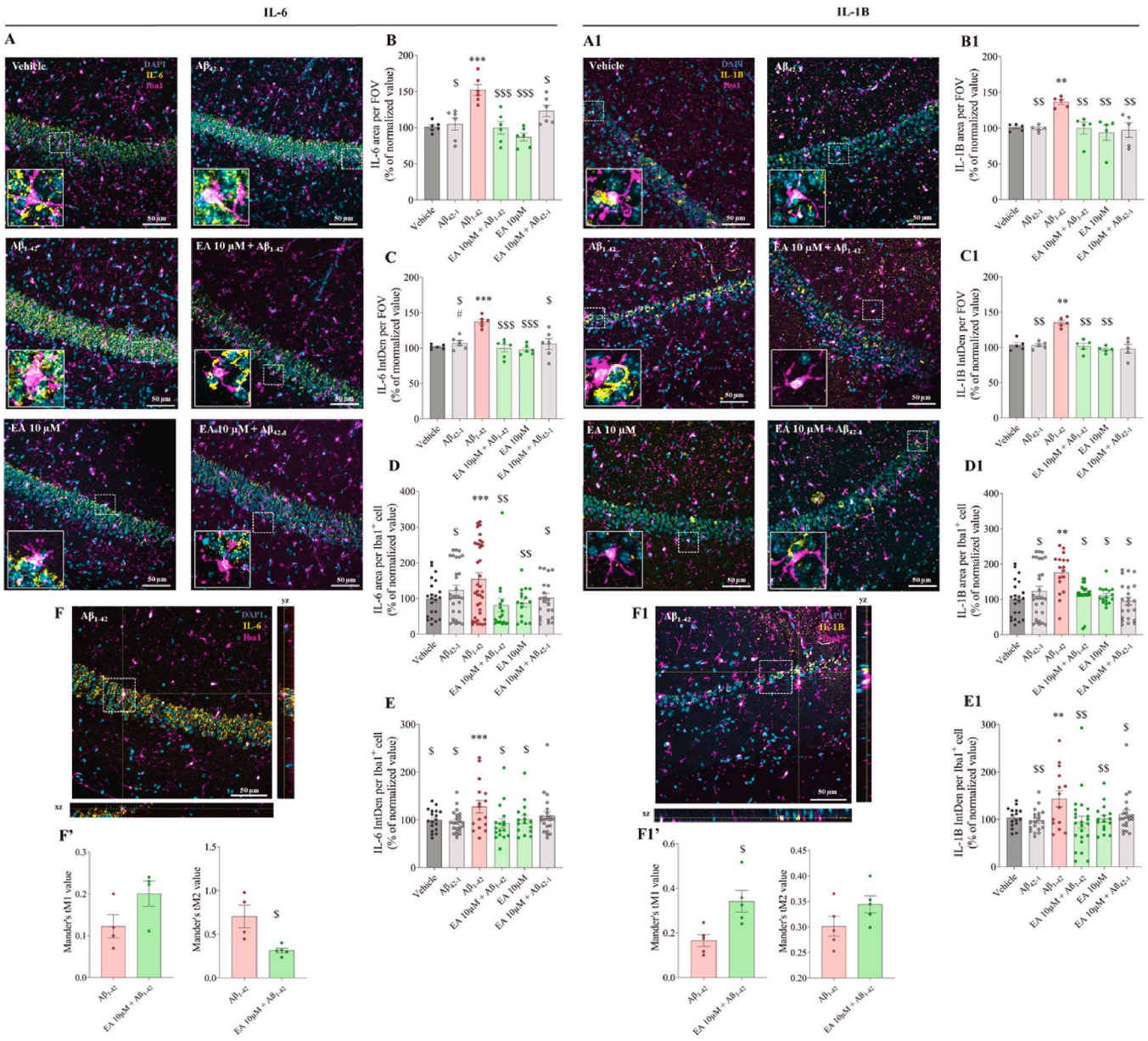


**Fig. 5. Ellagic acid attenuates Aβ$_{1-42}$-induced neuroinflammation by reducing IL-6 and IL-1β expression in microglia.** Statistical symbols: ***p < 0.001, **p < 0.01 vs. Vehicle; $p < 0.05, $$p < 0.01, $$$p < 0.001 vs. Aβ$_{1-42}$. Data represent mean ± SEM. (A, A1) Representative confocal images of CA1 hippocampal slices stained for Iba1 (magenta), DAPI (cyan), and either IL-6 (yellow, A) or IL-1β (yellow, A1). Insets show higher magnification of individual microglia. Scale bars = 50 μm. (B–C, B1–C1) Quantification of IL-6 IL-1β expression per field of view (FOV) (each dot represents the FOV, thereby the brain slices).(D-E, D1-E1) Quantification of cytokine expression per Iba1$^{+}$ cell, in terms of (D-D1) area and (E-E1) IntDen. Each dot represents a microglial cell. (F-F1) Representative and enlarged images to show the orthogonal side views along the XZ and XY planes from the confocal z-stack of the (F) IL-6/Iba1 and (F1) IL-1β/Iba1 confocal staining (Fiji, ImageJ, NIH, USA). (F′-F1′) Colocalization analysis using Manders' coefficients (M1 = fraction of IL-6 or IL-1β overlapping Iba1; M2 = fraction of Iba1 overlapping IL-6 or IL-1β), indicating reduced nuclear localization of cytokines following EA treatment. Each dot represents a FOV. (For interpretation of the references to colour in this figure legend, the reader is referred to the Web version of this article.)

expression levels of IL-1β$^{+}$ microglia cells (area Vehicle 61.05 ± 2.34, n=22, vs Aβ$_{1-42}$: 91.84 ± 4.32, n=17, p < 0.01; IntDen: Vehicle 64.99 ± 3.97, n=22, vs Aβ$_{1-42}$ 89.28 ± 2.62, n=17, p < 0.01; Fig. 5B1 and C1). Hence, this effects were prevented by EA pre-treatment (area: EA + Aβ$_{1-42}$ 59.89 ± 3.56, n=22, vs Aβ$_{1-42}$ 91.84 ± 4.32, n=17, p < 0.01; IntDen: EA + Aβ$_{1-42}$ 56.85 ± 3.17, n=22, vs Aβ$_{1-42}$: 89.28 ± 18.62, n=17, p < 0.05; Fig. 5D1 and E1). This pattern suggests that EA effectively attenuates both early vesicular inflammatory signalling and sustained cytokine overproduction by limiting the spatial spread of both IL-6 and Il-1β expression without diminishing the localized expression intensity.

To better understand the expression of interleukins within Iba$^{+}$ cells, colocalization analysis was performed using Manders' overlap coefficients (M1 and M2), which quantify the degree of spatial overlap between two fluorescent signals, independent of signal intensity (Manders et al., 1993), and this values as been calculated per FOV. In this context, M1 represents the fraction of IL-6 (or IL-1β) signal overlapping with the Iba1$^{+}$ microglial signal, while M2 reflects the fraction of Iba1 signal overlapping with the cytokine signal. In our study, EA pre-treatment significantly reduced both Manders' M1 (EA + Aβ$_{1-42}$ 0.10 ± 0.01, n = 4, vs Aβ$_{1-42}$ 0.17 ± 0.02, n = 4, p < 0.05; Fig. 5F') and M2 (EA + Aβ$_{1-42}$ 0.67 ± 0.02, n = 4, Aβ$_{1-42}$ 0.86 ± 0.04, n = 5, p < 0.05; Fig. 5F'). EA also attenuated IL-1β localization, as shown by decreased both Manders' coefficients (M1: EA + Aβ$_{1-42}$ 0.34 ± 0.82, n=5, Aβ$_{1-42}$ 0.15 ± 0.10, n=5, p<0.05; M2: EA + Aβ$_{1-42}$ 0.31 ± 0.76, n=5, Aβ$_{1-42}$

0.35 ± 0.50, n=5, p>0.05 Fig. 5F1'), indicating that, even though IL-6 (or IL-1β) expression is closely associated with Iba1$^+$ microglia across experimental conditions (Gosselin et al., 2017), it does not show strict intracellular co-localization with Iba1 within the microglial soma, reflected in the absence of perfect pixel overlap (Fig. S1, Supplementary material). Despite this, the consistent proximity supports a model in which activated microglia serve as a primary source of IL-6 (or IL-1β) secretion (Erta et al., 2012).

Together, these results demonstrate that EA reduces the number of cytokine-expressing microglia and their overall inflammatory phenotypes, while modulating cytokine spatial distribution and intracellular localization, suggesting its anti-inflammatory effects by regulating microglial activation and cytokine signalling at both the population and cellular levels, limiting neuroinflammatory progression.

### *3.6. Physicochemical characterization of empty and loaded EA-NSVs: an overview of stability overtime and in biological fluids as well as the in vitro EA release*

To bypass the pharmacokinetic issues herein we purpose an alternative drug delivery system as in previous studies of empty NSVs composed of Pluronic F-127, Span 85, and Cholesterol, and characterized in terms of physico-chemical properties to be potentially suitable for NtB delivery (Maisto et al., 2023). Based on this, EA was loaded into NSVs, and the resulting EA-NSVs were characterized in terms of hydrodynamic diameter, ζ-potential, PDI, anisotropy, drug entrapment efficiency (E.E.%), and *in-vitro* drug release (Table 2).

DLS results indicated an increase in hydrodynamic diameter (nm) for EA-NSVs compared to empty NSVs (EA-NSVs 223.0 ± 1.10, vs NSVs 163.4 ± 0.097, $p < 0.05$; Table 2), likely due to EA incorporation into the nanocarriers. Anisotropy experiments supported this data, showing an increase in bilayer anisotropy value for EA-NSVs (EA-NSVs 0.23, vs NSVs 0.15, $p < 0.05$; Table 2), probably due to the lipophilic nature of EA. Additionally, the ζ-potential of EA-NSVs showed a higher absolute value (EA-NSVs −18.5, vs NSVs −8.45, $p < 0.01$; Table 2), which might be attributed to the chemical structure of EA, orienting its hydroxyl groups near the head polar groups of the surfactant molecules on the nanocarriers' surface, thus altering the ζ-potential (Arulmozhi et al., 2013). Furthermore, DLS data demonstrated that the inclusion of EA did not affect the PDI value, which remained around 0.25. Specifically, a PDI value within the range of 0.1–0.3 indicates a narrow size distribution, confirming that both EA-NSVs and empty NSVs were monodisperse samples (Maisto et al., 2023).

Whereas, physicochemical stability over time was evaluated to determine the storage stability of samples for up to 45 days. Particularly, loaded EA-NSVs were stored at two temperatures, 4 °C and RT, and then they were analysed by DLS measurements in terms of hydrodynamic diameter and ζ-potential variations over 45 days. Results of physicochemical stability over time of empty NSVs are discussed in previous work (Maisto et al., 2023), in which data showed that empty NSVs were more stable at 4 °C in terms of hydrodynamic diameter, while RT size (nm) significantly increased during the experiment. In this case, even though the hydrodynamic diameter increases up to 45 days in both temperature cases (4 °C: 1day: 236.00 ± 1.10, n = 3, 15 days: 260.21 ± 2.11, n = 3, 30 days: 285.33 ± 1.33, n = 5, 45 days: 290.66 ± 1.45, $p < 0.01$; Fig. 6A and B), loaded EA-NSVs only at 4 °C can be considered stable as it still respects the size to be potentially intranasally delivered (Migliore et al., 2010).

By UV analysis, the entrapment efficiency value of EA-NSVs has been evaluated and it is possible to observe that the entrapped active compound is around 40 % which corresponds to 0.8 mg/ml (Table 2). The stability of EA entrapped inside the NSVs has been evaluated by UV analyses in terms of decomposition/degradation over time, up to 45 days, at two different storage temperatures (4°C and RT). The UV spectra were recorded immediately after sample preparation and after 15-30-45 days at two different temperatures (RT and 4 °C). By EA concentration values (0.8 mg/mL, E.E%: 40.66 ± 5.43, Table 2) it is possible to observe that the drug amount remains constant at 4 °C up to 30 days (1 day: 40.66 ± 5.43, n = 3, vs 30 days: 37.14 ± 3.57, n = 3, $p > 0.05$; Fig. 6D), suggesting that the nanocarriers component doesn't affect the EA chemical stability as well.

The system was also characterized to evaluate the effect of SNF and aCSF on the stability of EA-NSVs compared with empty ones in terms of the hydrodynamic diameter variations (by DLS measurements) for 3h as described in paragraph 2.5.2. Specifically, within the first hour a little decrease is observed (SNF: 0h 236.00 ± 1.10, n = 3, vs 1h 224.9 ± 2.11, n = 3, $p < 0.05$; aCSF: 0h 236.00 ± 1.10, n = 3, vs 1h 260.1 ± 4.24, n = 3, $p < 0.05$; Fig. 6C) probably for the system assessment in the new environment, while no significant variation of dimensions, always considering the intranasal delivery based characterization (Migliore et al., 2010), affect both samples up to 3h (SNF: 0h 236.00 ± 1.10, n = 3, vs 3h 250.1 ± 1.09, n = 3, $p < 0.01$; aCSF: 0h 236.00 ± 1.10, n = 3, vs 1h 262.9 ± 4.02, n = 3, $p < 0.01$; Fig. 6C). Thereby, it is possible to affirm that the media didn't affect the integrity of loaded niosomes, as well as the empty NSVs (Maisto et al., 2023).

To further support these results, morphology and stability of loaded EA-NSVs were also evaluated by Transmission Electronic Microscopy (TEM) analysis. Examination of the ultrastructure by TEM revealed that all vesicular preparations were non-aggregated almost spherical particles (Fig. S2). The morphology of niosomes revealed the presence of a well-identified unilamellar surface structure. Moreover, sizes appeared comparable to those recorded by DLS with a trend towards smaller sizes for niosomes dispersed in aCSF but with values within the range of measurements reported by DLS. A similar pattern of dispersed vesicles was visualized in all samples, indicating that all biological fluids do not affect the structure in terms of hydrodynamic diameter and phenomena degradation (Fig. S2).

*In vitro* release profile of EA-NSVs have been carried out in both Hepes (representing the control) and aCSF media, evaluating the effect of different media on the release capability of the NSVs over a period of up to 3 h, which corresponds to the potential residency time of nanocarriers in the nasal cavity (Maisto et al., 2023; Nair et al., 2021). In both media, the drug release is gradual and does not reach 100 % within 3 h (Hepes: 3h 19.87 ± 2.99, n = 3; aCSF 3h 30.98 ± 4.23, n = 3, Fig. S3), likely due to the lipophilic nature of EA and its interaction with the lipophilic bilayer structure of the vesicles (Sharma et al., 2015), suggesting that EA-NSVs function as a prolonged-release drug delivery system. Importantly, the biological activity of EA is not compromised in aCSF, as demonstrated by the electrophysiological results (paragraph 3.7), demonstrating that after incubation with *ex-vivo* hippocampal slices in aCSF, EA-NSVs exhibit a neuroprotective effect at low concentrations against $A\beta_{1\text{-}42}$ mediated LTP defects. Additionally, the chemical stability of EA in aCSF is maintained, as confirmed by UV spectrophotometer analysis, which still detected EA up to 3 h post-incubation, assuring its possible biological activity.

**Table 2**
**Physicochemical results.** Size (hydrodynamic diameter), charge (ζ-potential), PDI, entrapment efficiency (E.E.% and E.E mg/mL) and bilayer characterization in terms of anisotropy of loaded samples EA-NSVs. Listed values are determined as the mean value ± standard deviation of n = 3 EA-NSVs sample measurements.

| Sample | Hydrodynamic diameter (nm) ± SD | ζ-potential (mV) ± SD | PDI ± SD | E.E. (%) | E.E (mg/mL) | Anisotropy A.U. |
|---|---|---|---|---|---|---|
| EA-NSVs | 236.0 ± 1.10 | −18.5 ± 0.98 | 0.256 ± 0.002 | 40.66 ± 5.43 | 0.8 | 0.23 |

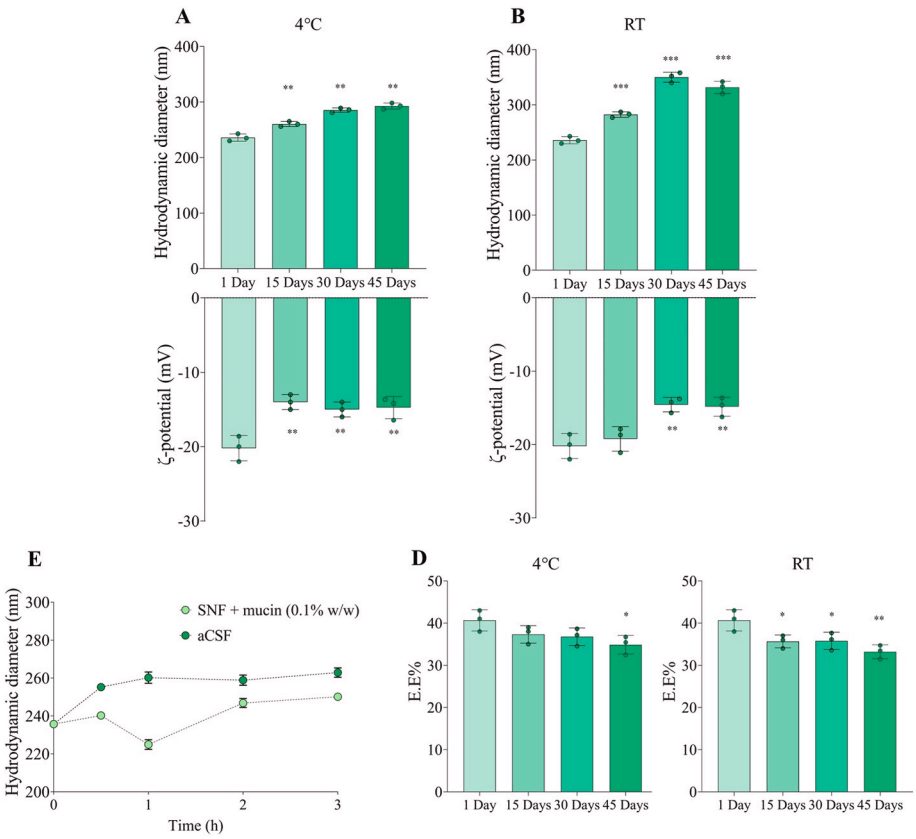


**Fig. 6. Physicochemical stability of empty and loaded niosomes.** Statistical symbols: *p < 0.05 **p < 0.01, and ***p < 0.001 vs 1 day. (A), (B) Results of investigation on physicochemical stability of loaded niosomes (EA-NSVs) in terms of hydrodynamic diameter (nm) and ζ-potential (mV) until up to 45 days: (A) at 4 °C; (B) at RT. Each dot represents the mean value of three measurements for each sample. (C) Stability studies following variation of hydrodynamic diameter values of loaded niosomes EA-NSVs: in the presence of SNF and mucin (0.1 % w/w), and in aCSF. Data are represented as the mean of three different samples ± SD. (D) Stability studies over time of E.E.% of loaded EA-NSVs at 2 different storage temperatures (4 °C and RT) over 45 days. Each dot represents the mean value of three measurements foreach sample.

### *3.7. EA-NSVs show neuroprotective effects at low concentrations against LTP defect Aβ$_{1-42}$ mediated*

To verify the neuroprotective effect of EA-NSVs we carried out synaptic plasticity experiments in *ex vivo* hippocampal slices pre-incubated with EA-NSVs and Aβ$_{1-42}$ (30 min). The dilutions of EA at 3 and 10 μM in 10 mL of aCSF were made considering the final concentration of EA in loaded EA-NSVs detected after UV-spectrophotometric analysis, and maintaining the concentrations of the NSVs components in the same surfactant concentration range (30 and 100 μM), that do not alter synaptic plasticity, as studied previously (Maisto et al., 2023). Indeed, as described in the previous work (Maisto et al., 2023), the degree of potentiation observed in *ex vivo* hippocampal slices pre-treated with empty NSVs was similar to that in the control group treated with the reverse oligomers Aβ$_{42-1}$ (Aβ$_{42-1}$ 157.04 ± 4.90, n = 7, vs NSVs 150.82 ± 3.04, n = 6, p > 0.05; Fig. 7A–B), confirming that the empty NSVs did not influence synaptic plasticity, either in presence of Aβ$_{1-42}$ (Aβ$_{42-1}$ 157.04 ± 4.90, n = 8, vs NSVs 150.82 ± 3.04, n = 5, p > 0.05; Aβ$_{1-42}$ 132.97 ± 2.56, n = 8, vs NSVs + Aβ$_{1-42}$ 124.41 ± 3.58, n = 5, p > 0.05; Fig. S3). In contrast, the EA-NSVs formulation demonstrated a significant neuroprotective effect at a lower concentration of 3 μM (EA-NSVs 3 μM + Aβ$_{1-42}$ 156.74 ± 4.44, n = 5, vs Aβ$_{1-42}$ 132.97 ± 2.56, n = 8, p < 0.001; Fig. 7A and B), indicating superior efficacy compared to free EA at the same concentration (EA 3 μM + Aβ$_{1-42}$ 132.97 + 2.56, n = 8, vs Aβ$_{1-42}$ 132.97 ± 2.56, n = 8, p > 0.05; EA-NSVs 3 μM + Aβ$_{1-42}$ 162.74 ± 8.44, n = 5, vs Aβ$_{1-42}$ 132.97 ± 2.56, n = 8, p < 0.001; Fig. 7A and B). Similarly, the EA-NSVs formulation at 10 μM also effectively restored LTP magnitude when co-incubated with Aβ$_{1-42}$ (EA-NSVs 10 μM + Aβ$_{1-42}$ 163.10 + 2.54, n = 6, vs Aβ$_{1-42}$ 132.97 ± 2.56, n = 8, p < 0.001; Fig. 7C and D), suggesting also that the pharmacological dose plateau has been reached.

## 4. Discussion

The need for new therapies is increasingly urgent, especially for neurodegenerative diseases like Alzheimer's disease (AD), and recently the attention is also focused on phytocompounds, due their pleiotropic activity, that can represent a source for new chemical structures to develop new therapeutics more specific. In this context, several studies have highlighted the neuroprotective effects and cognitive-enhancing effects of EA, demonstrating its ability to reduce oxidative stress, neuro-inflammation, and Aβ plaque formation (Jha et al., 2018; Li et al., 2025; Singh and Prasad, 2024) as well as its ability to prevent LTP deficits in brain inflammation (Chen et al., 2024; Farbood et al., 2015). However, in the literature, no evidence has been reported so far in terms of the effect of EA at neuronal and functional levels in an AD *ex vivo* model.

This study firstly investigated the EA's effect on synaptic plasticity at different concentration demonstrating that EA affects *per se* synaptic mechanisms at higher concentration, which was excluded in the further investigations. Consequently, it was evaluated the neuroprotective activity of EA on *ex vivo* synaptic plasticity function showing the rescue of Aβ$_{1-42}$-mediated alterations at the synaptic level in CA1 hippocampal pyramidal neurons in a dose-dependent manner, suggesting a restoration of synaptic defects associated with cognitive abilities consistent with behavioural data from previous studies (Jha et al., 2018; Li et al.,

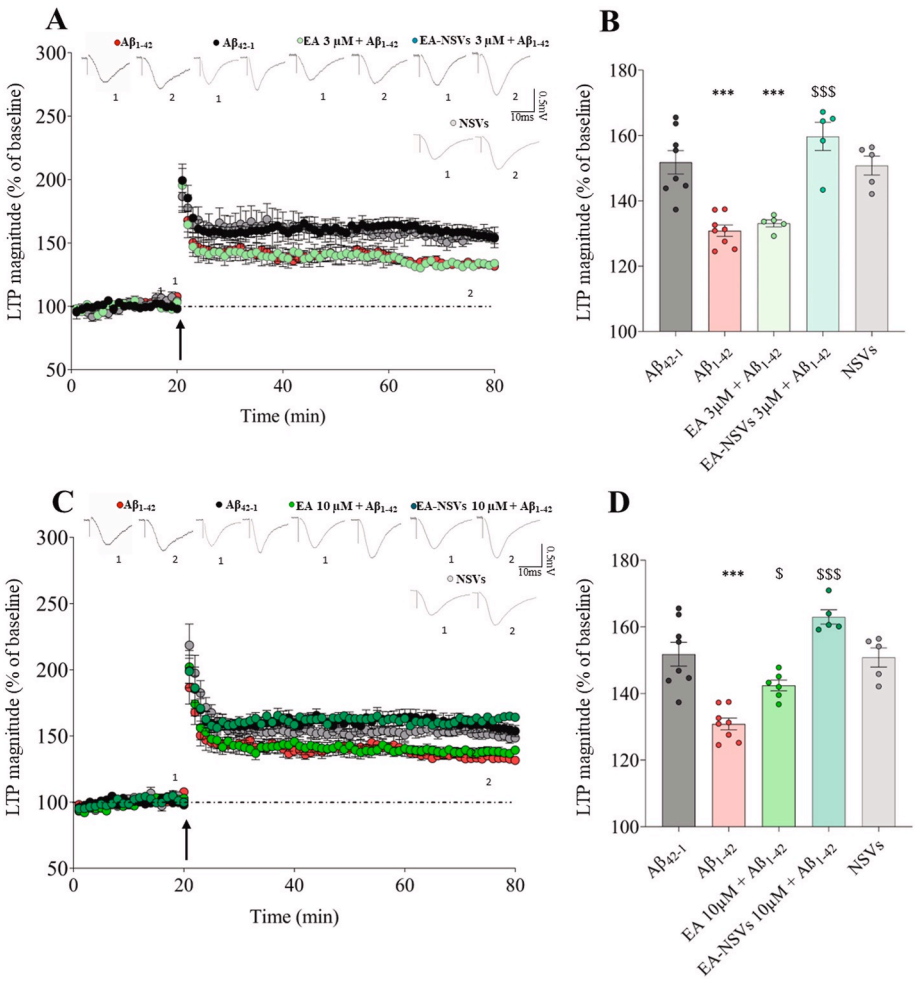


**Fig. 7. Loaded EA-NSVs reverse Aβ$_{1-42}$-mediated LTP impairment.** Statistic symbol: ***p < 0.001 vs Aβ$_{42-1}$,$p < 0.05, $$$p < 0.001 vs Aβ$_{1-42}$. Data are presented as mean ± SEM (A), (C) Above representative traces in respective experimental group: Aβ$_{1-42}$, Aβ$_{42-1}$, EA (3 and 10 μM) + Aβ$_{1-42}$, EA-NSVs EA (3 and 10 μM) + Aβ$_{1-42}$ and NSVs are shown; below summary graph of the averaged time course of LTP induced by theta-burst stimulation. (B), (D) Histograms illustrating the magnitude of LTP (% of baseline) in the respective experimental conditions. Dots represent the mean of last 10 min of LTP recorded for each brain slice.

2025; Singh and Prasad, 2024). Integrately, it is well known that accumulation of Aβ affects microglia by different mechanisms (Lau et al., 2021; Tiwari et al., 2019), and that microglial dysfunction results in synaptic alterations, LTP deficits and inadequate regenerative response (Neumann et al., 2008). In this context, we have previously demonstrated that microglia has internalized Aβ$_{1-42}$ continues to prune glutamatergic synapse, resulting in amyloid accumulation within glutamatergic synapses and contributing to the observed impairments in LTP and excitatory neurotransmission (Piccioni et al., 2024). Herein, EA was able to rescue the morphological alterations induced by *ex vivo* Aβ$_{1-42}$ incubation, all changes which are useful markers of inflammation and severity of damage (Green and Rowe, 2024). Specifically, Aβ exposure promoted a hypertrophic microglial phenotype, evidenced by increased soma area and perimeter alongside a reduced circularity index, features reminiscent of an inflammatory state (Godeanu and Cătălin, 2025; Murray et al., 2025; Vidal-Itriago et al., 2022). This was also confirmed by the number of intersections which, at larger radii, were higher with EA treatment, suggesting that EA restores microglia toward a more homeostatic state, characterized by reduced elongation and more homogeneous branching (Godeanu and Cătălin, 2025).

Such a phenotype is consistent with the concomitant cytokine profile observed, since activated inflammatory microglia typically engage NF-κB signalling and upregulate downstream pro-synthetic enzymes driving interleukins production (Kaltschmidt et al., 1994; Lau et al., 2021, p. 202; Streit et al., 2014). Indeed, to deeply investigate these morphological changes in correlation to the changes observed in neurotransmission, we have evaluated the interleukins expression, as IL-6 and IL-1β, which are involved in synaptic plasticity impairments (Del Rey et al., 2013; Gruol, 2015). Importantly, microglial morphology was paralleled by increased pro-inflammatory factors, whose labelling was often observed in close proximity to microglial processes rather than strictly localized to the soma, consistent with vesicular trafficking and secretion pathways (Erta et al., 2012; Gosselin et al., 2017). Excess of these interleukins may promote NMDA receptor internalization, thereby explaining the reduction of NMDA currents and LTP impairment observed (Tong et al., 2018; Viviani et al., 2003). EA treatment normalized microglial morphology, restored ramification, and reduced pro-inflammatory cytokine levels, maintaining the supportive microenvironment required for synaptic plasticity and supporting the view that EA's synaptic rescue deeply rely on its modulation of neuroimmune function.

Despite these promising results, the clinical translation of EA is constrained by its limited bioavailability (Murugan et al., 2009), as it exhibits poor systemic absorption and rapid metabolism, with the highest tissue concentrations found in the liver and kidneys rather than the brain (Murugan et al., 2009). Notably, gut-microbial conversion of EA leads to the formation of urolithins, metabolites reported to exert biological activity, including cognitive and synaptic neuroprotection (González-Barrio et al., 2010; González-Garrido et al., 2015; Mertens-Talcott et al., 2006; Seeram et al., 2006; Stoner et al., 2005; Yan et al.,

2014). Although, these metabolites could represent additional candidates for testing in our formulation, in this work we chose to focus on EA itself, investigating strategies to overcome its bioavailability issues and to explore its potential for targeted brain delivery, in light of *in vitro* studies using EA alone or in phytocomplexes on neuronal cells, or through non-oral administration routes that bypass gut microbiome metabolism (Abroumand Gholami et al., 2025; Banu and Das, 2025; Dessì et al., 2025). Specifically, we included EA in non-vesicular niosomes, and we characterized EA-NSVs formulation from a physicochemical perspective with a focus on intranasal delivery. In particular, we evaluated the hydrodynamic diameter, a key parameter for efficient transport across the nasal mucosa and subsequent delivery to the brain via the olfactory and trigeminal pathways (Adnet et al., 2020; Migliore et al., 2010), along with other parameters relevant to formulation stability. Consistent with previous findings (Rinaldi et al., 2019), the carrier exhibited properties well suited for intranasal delivery. The particle size, in particular, falls within the optimal range for passage through the nasal epithelium and potential uptake via olfactory pathways. While our *ex vivo* system does not allow assessment of blood–brain barrier penetration, pharmacokinetics, or *in vivo* intranasal delivery, this encapsulation significantly improved the efficacy of EA compared with the free compound. The activity of EA-NSVs observed at concentrations to whom free EA wasn't effective is likely attributable to improved solubility, membrane interaction, and sustained release (Bhardwaj et al., 2020), as also supported by our release profiling in aCSF or TEM analysis, without compromising the integrity of EA-NSVs either. These effects explain the greater neuroprotection without invoking BBB penetration, which remains to be further investigated *in vivo*.

Collectively, our findings, based on a well-known *ex vivo* model (Chen et al., 2006; Mango et al., 2016; Piccioni et al., 2021; Varga et al., 2015; Wang et al., 2004; Yao et al., 2013), support the neuroprotective effect of EA counters $A\beta_{1\text{-}42}$-induced cognitive impairment through stabilization of glutamatergic synapse and attenuation of microglia-derived cytokine signaling. Encapsulation into nanovesicles enhances these protective actions by improving drug stability and releasing kinetics. Nevertheless, while the characterization of NSVs was based on the intranasal delivery, future prospectives will include *in vivo* studies to validate EA-NSVs distribution, pharmacokinetics, and therapeutic efficiency following nose to brain delivery.

## 5. Conclusions

In this study, EA demonstrated robust effects on synaptic plasticity and neuroinflammatory markers in an *ex vivo* model of $A\beta_{1\text{-}42}$-induced impairment, highlighting a protective mechanism closely linked to modulation of microglial activity and cytokine signaling. These results provide strong evidence that EA can pharmacologically rescue synaptic dysfunction under neuroinflammatory conditions.

Despite these promising effects, the clinical translation of EA is limited by its poor bioavailability and metabolic instability. To address these challenges, we developed EA-NSVs, a biocompatible formulation that enhances EA stability, solubility, and sustained release. Importantly, EA-NSVs produced neuroprotective effects at lower concentrations than free EA in the *ex vivo* system, supporting their potential to improve therapeutic efficacy.

While the present findings are confined to an *ex vivo* model, they establish a rationale for future *in vivo* investigations. Subsequent studies will aim to validate the pharmacokinetic, brain distribution, and functional efficacy of EA-NSVs, including also comparisons with EA metabolites, such as urolithins, given the versatility of our drug delivery system. Collectively, these results position EA, particularly in niosomal form, as a promising candidate for strategies aimed at mitigating synaptic and cognitive deficits associated with neurodegenerative diseases.

## CRediT authorship contribution statement

**Nunzia Maisto:** Writing – review & editing, Writing – original draft, Validation, Project administration, Methodology, Investigation, Data curation, Conceptualization. **Sepideh Dashtiani:** Investigation. **Jacopo Forte:** Investigation. **Maria Grazia Ammendolia:** Writing – original draft, Investigation, Data curation. **Viviana Triaca:** Writing – review & editing, Visualization, Supervision, Conceptualization. **Federica Rinaldi:** Writing – review & editing, Supervision, Conceptualization. **Dalila Mango:** Writing – review & editing, Visualization, Validation, Supervision, Project administration, Methodology, Data curation, Conceptualization.

## Declaration of competing interest

The authors declare no conflict of interest.

## Appendix A. Supplementary data

Supplementary data to this article can be found online at https://doi.org/10.1016/j.ejphar.2025.178317.

## Data availability

We confirm that all the data are published in the article and in its supplementary file.

## References

Abbott, N.J., Patabendige, A.A.K., Dolman, D.E.M., Yusof, S.R., Begley, D.J., 2010. Structure and function of the blood–brain barrier. Neurobiol. Dis. 37, 13–25. https://doi.org/10.1016/j.nbd.2009.07.030.

Abroumand Gholami, A., Rahmani, S., Moharreri, P., Amirazodi, E., Molavi, A.M., Mokhtari, T., Tahmasebi, F., Rabiei Rad, A., Babaloo, H., 2025. Liposomal ellagic acid enhances the regenerative potential of ADMSC-laden nanofibrous PCL scaffolds in a rat model of spinal cord injury. Sci. Rep. 15, 30202. https://doi.org/10.1038/s41598-025-15789-w.

Adnet, T., Groo, A.-C., Picard, C., Davis, A., Corvaisier, S., Since, M., Bounoure, F., Rochais, C., Le Pluart, L., Dallemagne, P., Malzert-Fréon, A., 2020. Pharmacotechnical development of a nasal drug delivery composite nanosystem intended for alzheimer's disease treatment. Pharmaceutics 12, 251. https://doi.org/10.3390/pharmaceutics12030251.

Ahmed, T., N. Setzer, W., Fazel Nabavi, S., Erdogan Orhan, I., Braidy, N., Sobarzo-Sanchez, E., Mohammad Nabavi, S., 2016. Insights into effects of ellagic acid on the nervous system: a mini review. Curr. Pharm. Des. 22, 1350–1360. https://doi.org/10.2174/1381612822666160125114503.

Anderson, D.M., Hall, L.L., Ayyalapu, A.R., Irion, V.R., Nantz, M.H., Hecker, J.G., 2003. Stability of mRNA/cationic lipid lipoplexes in human and rat cerebrospinal fluid: methods and evidence for nonviral mRNA gene delivery to the central nervous system. Hum. Gene Ther. 14, 191–202. https://doi.org/10.1089/10430340360535751.

Arshadi, C., Günther, U., Eddison, M., Harrington, K.I.S., Ferreira, T.A., 2021. SNT: a unifying toolbox for quantification of neuronal anatomy. Nat. Methods 18, 374–377. https://doi.org/10.1038/s41592-021-01105-7.

Arulmozhi, V., Pandian, K., Mirunalini, S., 2013. Ellagic acid encapsulated chitosan nanoparticles for drug delivery system in human oral cancer cell line (KB). Colloids Surf. B Biointerfaces 110, 313–320. https://doi.org/10.1016/j.colsurfb.2013.03.039.

Atta-Ur-Rahman, Ngounou, F.N., Choudhary, M.I., Malik, S., Makhmoor, T., Nur-E-Alam, M., Zareen, S., Lontsi, D., Ayafor, J.F., Sondengam, B.L., 2001. New antioxidant and antimicrobial ellagic acid derivatives from pteleopsis hylodendron. Planta Med. 67, 335–339. https://doi.org/10.1055/s-2001-14306.

Banu, Z., Das, N.R., 2025. In vitro assessment of cholinesterase inhibition and neuroprotective effects of Elaeocarpus angustifolius blume against amyloid-beta peptide-induced toxicity in SH-SY5Y and BV-2 cells. Neurochem. Res. 50, 226. https://doi.org/10.1007/s11064-025-04478-9.

Bartelds, R., Nematollahi, M.H., Pols, T., Stuart, M.C.A., Pardakhty, A., Asadikaram, G., Poolman, B., 2018. Niosomes, an alternative for liposomal delivery. PLoS One 13, e0194179. https://doi.org/10.1371/journal.pone.0194179.

Bhardwaj, P., Tripathi, P., Gupta, R., Pandey, S., 2020. Niosomes: a review on niosomal research in the last decade. J. Drug Deliv. Sci. Technol. 56, 101581. https://doi.org/10.1016/j.jddst.2020.101581.

Chapman, P.F., White, G.L., Jones, M.W., Cooper-Blacketer, D., Marshall, V.J., Irizarry, M., Younkin, L., Good, M.A., Bliss, T.V.P., Hyman, B.T., Younkin, S.G., Hsiao, K.K., 1999. Impaired synaptic plasticity and learning in aged amyloid precursor protein transgenic mice. Nat. Neurosci. 2, 271–276. https://doi.org/10.1038/6374.

Chen, F., Lu, K., Bai, N., Hao, Y., Wang, H., Zhao, X., Yue, F., 2024. Oral administration of ellagic acid mitigates perioperative neurocognitive disorders, hippocampal oxidative stress, and neuroinflammation in aged mice by restoring IGF-1 signaling. Sci. Rep. 14, 2509. https://doi.org/10.1038/s41598-024-53127-8.

Chen, L., Yamada, K., Nabeshima, T., Sokabe, M., 2006. α7 nicotinic acetylcholine receptor as a target to rescue deficit in hippocampal LTP induction in β-amyloid infused rats. Neuropharmacology 50, 254–268. https://doi.org/10.1016/j.neuropharm.2005.09.018.

Chen, Q.-S., Kagan, B.L., Hirakura, Y., Xie, C.-W., 2000. Impairment of hippocampal long-term potentiation by alzheimer amyloid ?-peptides. J. Neurosci. Res. 60, 65–72. https://doi.org/10.1002/(SICI)1097-4547(20000401)60:1%253C65::AID-JNR7%253E3.0.CO;2-Q.

Corsaro, R., Lombardo, R., Ghelardini, C., Di Cesare Mannelli, L., Bani, D., Bonaccorso, A., Pignatello, R., 2022. Development of eudragit® nanoparticles for intranasal drug delivery: preliminary technological and toxicological evaluation. Appl. Sci. 12, 2373. https://doi.org/10.3390/app12052373.

De Jaco, A., Mango, D., De Angelis, F., Favaloro, F., Andolina, D., Nisticò, R., Fiori, E., Colamartino, M., Pascucci, T., 2017. Unbalance between excitation and inhibition in phenylketonuria, a genetic metabolic disease associated with autism. Int. J. Mol. Sci. 18, 941. https://doi.org/10.3390/ijms18050941.

Del Rey, A., Balschun, D., Wetzel, W., Randolf, A., Besedovsky, H.O., 2013. A cytokine network involving brain-borne IL-1β, IL-1ra, IL-18, IL-6, and TNFα operates during long-term potentiation and learning. Brain Behav. Immun. 33, 15–23. https://doi.org/10.1016/j.bbi.2013.05.011.

Dessì, D., Fais, G., Follesa, P., Sarais, G., 2025. Neuroprotective effects of myrtle berry By-Product extracts on 6-OHDA-Induced cytotoxicity in PC12 cells. Antioxid. Basel Switz. 14, 88. https://doi.org/10.3390/antiox14010088.

Dionísio, P.A., Amaral, J.D., Ribeiro, M.F., Lo, A.C., D'Hooge, R., Rodrigues, C.M.P., 2015. Amyloid-β pathology is attenuated by tauroursodeoxycholic acid treatment in APP/PS1 mice after disease onset. Neurobiol. Aging 36, 228–240. https://doi.org/10.1016/j.neurobiolaging.2014.08.034.

Erta, M., Quintana, A., Hidalgo, J., 2012. Interleukin-6, a major cytokine in the central nervous system. Int. J. Biol. Sci. 8, 1254–1266. https://doi.org/10.7150/ijbs.4679.

Farbood, Y., Sarkaki, A., Dianat, M., Khodadadi, A., Haddad, M.K., Mashhadizadeh, S., 2015. Ellagic acid prevents cognitive and hippocampal long-term potentiation deficits and brain inflammation in rat with traumatic brain injury. Life Sci. 124, 120–127. https://doi.org/10.1016/j.lfs.2015.01.013.

Feng, Y., Yang, S., Du, X., Zhang, X., Sun, X., Zhao, M., Sun, G., Liu, R., 2009. Ellagic acid promotes Aβ42 fibrillization and inhibits Aβ42-induced neurotoxicity. Biochem. Biophys. Res. Commun. 390, 1250–1254. https://doi.org/10.1016/j.bbrc.2009.10.130.

Giuli, M.V., Hanieh, P.N., Forte, J., Fabiano, M.G., Mancusi, A., Natiello, B., Rinaldi, F., Del Favero, E., Ammendolia, M.G., Marianecci, C., Checquolo, S., Carafa, M., 2024. pH-sensitive niosomes for ATRA delivery: a promising approach to inhibit Pin1 in high-grade serous ovarian cancer. Int. J. Pharm. 649, 123672. https://doi.org/10.1016/j.ijpharm.2023.123672.

Godeanu, S., Cătălin, B., 2025. The complementary role of morphology in understanding microglial functional heterogeneity. Int. J. Mol. Sci. 26, 3811. https://doi.org/10.3390/ijms26083811.

González-Barrio, R., Borges, G., Mullen, W., Crozier, A., 2010. Bioavailability of anthocyanins and ellagitannins following consumption of raspberries by healthy humans and subjects with an ileostomy. J. Agric. Food Chem. 58, 3933–3939. https://doi.org/10.1021/jf100315d.

González-Garrido, A., Vega, R., Mercado, F., López, I.A., Soto, E., 2015. Acid-sensing ion channels expression, identity and role in the excitability of the cochlear afferent neurons. Front. Cell. Neurosci. 9. https://doi.org/10.3389/fncel.2015.00483.

Goshen, I., Kreisel, T., Ounallah-Saad, H., Renbaum, P., Zalzstein, Y., Ben-Hur, T., Levy-Lahad, E., Yirmiya, R., 2007. A dual role for interleukin-1 in hippocampal-dependent memory processes. Psychoneuroendocrinology 32, 1106–1115. https://doi.org/10.1016/j.psyneuen.2007.09.004.

Gosselin, D., Skola, D., Coufal, N.G., Holtman, I.R., Schlachetzki, J.C.M., Sajti, E., Jaeger, B.N., O'Connor, C., Fitzpatrick, C., Pasillas, M.P., Pena, M., Adair, A., Gonda, D.D., Levy, M.L., Ransohoff, R.M., Gage, F.H., Glass, C.K., 2017. An environment-dependent transcriptional network specifies human microglia identity. Science 356, eaal3222. https://doi.org/10.1126/science.aal3222.

Green, T.R.F., Rowe, R.K., 2024. Quantifying microglial morphology: an insight into function. Clin. Exp. Immunol. 216, 221–229. https://doi.org/10.1093/cei/uxae023.

Gruol, D.L., 2015. IL-6 regulation of synaptic function in the CNS. Neuropharmacology 96, 42–54. https://doi.org/10.1016/j.neuropharm.2014.10.023.

Haass, C., Selkoe, D., 2022. If amyloid drives alzheimer disease, why have anti-amyloid therapies not yet slowed cognitive decline? PLoS Biol. 20, e3001694. https://doi.org/10.1371/journal.pbio.3001694.

Harry, G.J., Kraft, A.D., 2008. Neuroinflammation and microglia: considerations and approaches for neurotoxicity assessment. Expert Opin. Drug Metab. Toxicol. 4, 1265–1277. https://doi.org/10.1517/17425255.4.10.1265.

Huang, Q., Chen, Y., Zhang, W., Xia, X., Li, H., Qin, M., Gao, H., 2024. Nanotechnology for enhanced nose-to-brain drug delivery in treating neurological diseases. J. Contr. Release 366, 519–534. https://doi.org/10.1016/j.jconrel.2023.12.054.

Javaid, N., Shah, M.A., Rasul, A., Chauhdary, Z., Saleem, U., Khan, H., Ahmed, N., Uddin, MdS., Mathew, B., Behl, T., Blundell, R., 2021. Neuroprotective effects of ellagic acid in alzheimer's disease: focus on underlying molecular mechanisms of therapeutic potential. Curr. Pharm. Des. 27, 3591–3601. https://doi.org/10.2174/1381612826666201112144006.

Jha, A.B., Panchal, S.S., Shah, A., 2018. Ellagic acid: insights into its neuroprotective and cognitive enhancement effects in sporadic Alzheimer's disease. Pharmacol. Biochem. Behav. 175, 33–46. https://doi.org/10.1016/j.pbb.2018.08.007.

Kaltschmidt, C., Kaltschmidt, B., Lannes-Vieira, J., Kreutzberg, G.W., Wekerle, H., Baeuerle, P.A., Gehrmann, J., 1994. Transcription factor NF-κB is activated in microglia during experimental autoimmune encephalomyelitis. J. Neuroimmunol. 55, 99–106. https://doi.org/10.1016/0165-5728(94)90151-1.

Khalin, I., Alyautdin, R., Ismail, N.M., Haron, M.H., Kuznetsov, D., 2014. Nanoscale drug delivery systems and the blood–brain barrier. Int. J. Nanomed. 795. https://doi.org/10.2147/IJN.S52236.

Khan, S., Barve, K.H., Kumar, M.S., 2020. Recent advancements in pathogenesis, diagnostics and treatment of alzheimer's disease. Curr. Neuropharmacol. 18, 1106–1125. https://doi.org/10.2174/1570159X18666200528142429.

Kiasalari, Z., Heydarifard, R., Khalili, M., Afshin-Majd, S., Baluchnejadmojarad, T., Zahedi, E., Sanaierad, A., Roghani, M., 2017. Ellagic acid ameliorates learning and memory deficits in a rat model of Alzheimer's disease: an exploration of underlying mechanisms. Psychopharmacology (Berl.) 234, 1841–1852. https://doi.org/10.1007/s00213-017-4589-6.

Lau, S.-F., Fu, A.K.Y., Ip, N.Y., 2021. Cytokine signaling convergence regulates the microglial state transition in Alzheimer's disease. Cell. Mol. Life Sci. 78, 4703–4712. https://doi.org/10.1007/s00018-021-03810-0.

Lentz, B.R., 1989. Membrane "fluidity" as detected by diphenylhexatriene probes. Chem. Phys. Lipids 50, 171–190. https://doi.org/10.1016/0009-3084(89)90049-2.

Li, Y., Zhang, J., Zhang, L., Hu, C., Zhou, L., Cheng, Y., Liu, Q., 2025. Ellagic acid(EA) ameliorates Alzheimer's disease by reducing Aβ levels, oxidative stress and attenuating inflammation. Eur. J. Pharmacol. 986, 177099. https://doi.org/10.1016/j.ejphar.2024.177099.

Li, Z., Yu, H., Liu, C., Wang, C., Zeng, X., Yan, J., Sun, Y., 2023. Efficiency co-delivery of ellagic acid and oxygen by a non-invasive liposome for ameliorating diabetic retinopathy. Int. J. Pharm. 641, 122987. https://doi.org/10.1016/j.ijpharm.2023.122987.

Maisto, N., Mango, D., Bettucci, A., Barbato, G., Ammendolia, M.G., Rinaldi, F., Marianecci, C., Nisticò, R., Carafa, M., 2023. FUS and surfactant-based nanocarriers: a combined strategy for nose to brain drug delivery. J. Drug Deliv. Sci. Technol., 104977 https://doi.org/10.1016/j.jddst.2023.104977.

Manders, E.M.M., Verbeek, F.J., Aten, J.A., 1993. Measurement of co-localization of objects in dual-colour confocal images. J. Microsc. 169, 375–382. https://doi.org/10.1111/j.1365-2818.1993.tb03313.x.

Mango, D., Weisz, F., Nisticò, R., 2016. Ginkgolic acid protects against Aβ-Induced synaptic dysfunction in the hippocampus. Front. Pharmacol. 7. https://doi.org/10.3389/fphar.2016.00401.

Marianecci, C., Petralito, S., Rinaldi, F., Hanieh, P.N., Carafa, M., 2016. Some recent advances on liposomal and niosomal vesicular carriers. J. Drug Deliv. Sci. Technol. 32, 256–269. https://doi.org/10.1016/j.jddst.2015.10.008.

Martinez, A., Hériché, J.-K., Calvo, M., Tischer, C., Otxoa-de-Amezaga, A., Pedragosa, J., Bosch, A., Planas, A.M., Petegnief, V., 2023. Characterization of microglia behaviour in healthy and pathological conditions with image analysis tools. Open Biol. 13, 220200. https://doi.org/10.1098/rsob.220200.

Mecca, A.P., O'Dell, R.S., Sharp, E.S., Banks, E.R., Bartlett, H.H., Zhao, W., Lipior, S., Diepenbrock, N.G., Chen, M., Naganawa, M., Toyonaga, T., Nabulsi, N.B., Vander Wyk, B.C., Arnsten, A.F.T., Huang, Y., Carson, R.E., Van Dyck, C.H., 2022. Synaptic density and cognitive performance in Alzheimer's disease: a PET imaging study with [ $^{11}$ C]UCB-J. Alzheimer's Dement. 18, 2527–2536. https://doi.org/10.1002/alz.12582.

Mertens-Talcott, S.U., Jilma-Stohlawetz, P., Rios, J., Hingorani, L., Derendorf, H., 2006. Absorption, metabolism, and antioxidant effects of pomegranate (*Punica granatum* L.) polyphenols after ingestion of a standardized extract in healthy human volunteers. J. Agric. Food Chem. 54, 8956–8961. https://doi.org/10.1021/jf061674h.

Migliore, M.M., Vyas, T.K., Campbell, R.B., Amiji, M.M., Waszczak, B.L., 2010. Brain delivery of proteins by the intranasal route of administration: a comparison of cationic liposomes versus aqueous solution formulations. J. Pharm. Sci. 99, 1745–1761. https://doi.org/10.1002/jps.21939.

Monfort, P., Felipo, V., 2010. Amyloid-β impairs, and ibuprofen restores, the cGMP pathway, synaptic expression of AMPA receptors and long-term potentiation in the hippocampus. J. Alzheimers Dis. 22, 795–809. https://doi.org/10.3233/JAD-2010-101092.

Murray, C.J., Tunderman, E.D., Vecchiarelli, H.A., González Ibáñez, F., Tremblay, M.-È., 2025. A comparison of microglial morphological complexity in adult mouse brain samples using 2-dimensional and 3-dimensional image analysis tools. Glial Health Res 2, 100007. https://doi.org/10.1016/j.ghres.2025.100007.

Murugan, V., Mukherjee, K., Maiti, K., Mukherjee, P.K., 2009. Enhanced oral bioavailability and antioxidant profile of ellagic acid by phospholipids. J. Agric. Food Chem. 57, 4559–4565. https://doi.org/10.1021/jf8037105.

Nair, S.C., Vinayan, K.P., Mangalathillam, S., 2021. Nose to brain delivery of phenytoin sodium loaded nano lipid carriers: formulation, drug release, permeation and in vivo pharmacokinetic studies. Pharmaceutics 13, 1640. https://doi.org/10.3390/pharmaceutics13101640.

Neumann, H., Kotter, M.R., Franklin, R.J.M., 2008. Debris clearance by microglia: an essential link between degeneration and regeneration. Brain 132, 288–295. https://doi.org/10.1093/brain/awn109.

Nisticò, R., Pignatelli, M., Piccinin, S., Mercuri, N.B., Collingridge, G., 2012. Targeting synaptic dysfunction in alzheimer's disease therapy. Mol. Neurobiol. 46, 572–587. https://doi.org/10.1007/s12035-012-8324-3.

Piccioni, G., Maisto, N., d'Ettorre, A., Strimpakos, G., Nisticò, R., Triaca, V., Mango, D., 2024. Switch to phagocytic microglia by CSFR1 inhibition drives amyloid-beta clearance from glutamatergic terminals rescuing LTP in acute hippocampal slices. Transl. Psychiatry 14, 338. https://doi.org/10.1038/s41398-024-03019-2.

Piccioni, G., Mango, D., Saidi, A., Corbo, M., Nisticò, R., 2021. Targeting microglia-synapse interactions in alzheimer's disease. Int. J. Mol. Sci. 22, 2342. https://doi.org/10.3390/ijms22052342.

Puzzo, D., Vitolo, O., Trinchese, F., Jacob, J.P., Palmeri, A., Arancio, O., 2005. Amyloid-β peptide inhibits activation of the nitric Oxide/cGMP/cAMP-responsive element-binding protein pathway during hippocampal synaptic plasticity. J. Neurosci. 25, 6887–6897. https://doi.org/10.1523/JNEUROSCI.5291-04.2005.

Reddaway, J., Richardson, P.E., Bevan, R.J., Stoneman, J., Palombo, M., 2023. Microglial morphometric analysis: so many options, so little consistency. Front. Neuroinf. 17, 1211188. https://doi.org/10.3389/fninf.2023.1211188.

Rinaldi, F., Seguella, L., Gigli, S., Hanieh, P.N., Del Favero, E., Cantù, L., Pesce, M., Sarnelli, G., Marianecci, C., Esposito, G., Carafa, M., 2019. inPentasomes: an innovative nose-to-brain pentamidine delivery blunts MPTP parkinsonism in mice. J. Contr. Release 294, 17–26. https://doi.org/10.1016/j.jconrel.2018.12.007.

Rowan, M.J., Klyubin, I., Cullen, W.K., Anwyl, R., 2003. Synaptic plasticity in animal models of early Alzheimer's disease. Philos. Trans. R. Soc. Lond. B Biol. Sci. 358, 821–828. https://doi.org/10.1098/rstb.2002.1240.

Saed, B., Ramseier, N.T., Perera, T., Anderson, J., Burnett, J., Gunasekara, H., Burgess, A., Jing, H., Hu, Y.S., 2024. Increased vesicular dynamics and nanoscale clustering of IL-2 after T cell activation. Biophys. J. 123, 2343–2353. https://doi.org/10.1016/j.bpj.2024.03.029.

Sanadgol, N., Golab, F., Tashakkor, Z., Taki, N., Moradi Kouchi, S., Mostafaie, A., Mehdizadeh, M., Abdollahi, M., Taghizadeh, G., Sharifzadeh, M., 2017. Neuroprotective effects of ellagic acid on cuprizone-induced acute demyelination through limitation of microgliosis, adjustment of CXCL12/IL-17/IL-11 axis and restriction of mature oligodendrocytes apoptosis. Pharm. Biol. 55, 1679–1687. https://doi.org/10.1080/13880209.2017.1319867.

Seeram, N.P., Henning, S.M., Zhang, Y., Suchard, M., Li, Z., Heber, D., 2006. Pomegranate juice ellagitannin metabolites are present in human plasma and some persist in urine for up to 48 hours. J. Nutr. 136, 2481–2485. https://doi.org/10.1093/jn/136.10.2481.

Shankar, G.M., Li, S., Mehta, T.H., Garcia-Munoz, A., Shepardson, N.E., Smith, I., Brett, F. M., Farrell, M.A., Rowan, M.J., Lemere, C.A., Regan, C.M., Walsh, D.M., Sabatini, B. L., Selkoe, D.J., 2008. Amyloid-β protein dimers isolated directly from Alzheimer's brains impair synaptic plasticity and memory. Nat. Med. 14, 837–842. https://doi.org/10.1038/nm1782.

Sharma, V., Anandhakumar, S., Sasidharan, M., 2015. Self-degrading niosomes for encapsulation of hydrophilic and hydrophobic drugs: an efficient carrier for cancer multi-drug delivery. Mater. Sci. Eng. C 56, 393–400. https://doi.org/10.1016/j.msec.2015.06.049.

Sierra, A., Miron, V.E., Paolicelli, R.C., Ransohoff, R.M., 2024. Microglia in health and diseases: integrative hubs of the central nervous system (CNS). Cold Spring Harb. Perspect. Biol. 16, a041366. https://doi.org/10.1101/cshperspect.a041366.

Singh, N.A.K., Prasad, S., 2024. Ellagic acid reverses alterations in the expression of AMPA receptor and its scaffolding proteins in the cerebral cortex and memory decline in STZ-sporadic alzheimer' s disease mouse model. Psychopharmacology (Berl.). https://doi.org/10.1007/s00213-024-06622-9.

Snyder, E.M., Nong, Y., Almeida, C.G., Paul, S., Moran, T., Choi, E.Y., Nairn, A.C., Salter, M.W., Lombroso, P.J., Gouras, G.K., Greengard, P., 2005. Regulation of NMDA receptor trafficking by amyloid-β. Nat. Neurosci. 8, 1051–1058. https://doi.org/10.1038/nn1503.

Stoner, G.D., Sardo, C., Apseloff, G., Mullet, D., Wargo, W., Pound, V., Singh, A., Sanders, J., Aziz, R., Casto, B., Sun, X., 2005. Pharmacokinetics of anthocyanins and ellagic acid in healthy volunteers fed freeze-dried black raspberries daily for 7 days. J. Clin. Pharmacol. 45, 1153–1164. https://doi.org/10.1177/0091270005279636.

Streit, W.J., Xue, Q.-S., Tischer, J., Bechmann, I., 2014. Microglial pathology. Acta Neuropathol. Commun. 2, 142. https://doi.org/10.1186/s40478-014-0142-6.

Tancredi, V., D'Antuono, M., Cafè, C., Giovedì, S., Buè, M.C., D'Arcangelo, G., Onofri, F., Benfenati, F., 2000. The inhibitory effects of Interleukin-6 on synaptic plasticity in the rat hippocampus are associated with an inhibition of mitogen-activated protein kinase ERK. J. Neurochem. 75, 634–643. https://doi.org/10.1046/j.1471-4159.2000.0750634.x.

Terry, R.D., Masliah, E., Salmon, D.P., Butters, N., DeTeresa, R., Hill, R., Hansen, L.A., Katzman, R., 1991. Physical basis of cognitive alterations in alzheimer's disease: synapse loss is the major correlate of cognitive impairment. Ann. Neurol. 30, 572–580. https://doi.org/10.1002/ana.410300410.

Tiwari, S., Atluri, V., Kaushik, A., Yndart, A., Nair, M., 2019. Alzheimer's disease: pathogenesis, diagnostics, and therapeutics. Int. J. Nanomed. 14, 5541–5554. https://doi.org/10.2147/IJN.S200490.

Tong, L., Prieto, G.A., Cotman, C.W., 2018. IL-1β suppresses cLTP-induced surface expression of GluA1 and actin polymerization via ceramide-mediated src activation. J. Neuroinflammation 15, 127. https://doi.org/10.1186/s12974-018-1158-9.

Varga, E., Juhász, G., Bozsó, Z., Penke, B., Fülöp, L., Szegedi, V., 2015. Amyloid-β1-42 disrupts synaptic plasticity by altering glutamate recycling at the synapse. J. Alzheimers Dis. 45, 449–456. https://doi.org/10.3233/JAD-142367.

Vidal-Itriago, A., Radford, R.A.W., Aramideh, J.A., Maurel, C., Scherer, N.M., Don, E.K., Lee, A., Chung, R.S., Graeber, M.B., Morsch, M., 2022. Microglia morphophysiological diversity and its implications for the CNS. Front. Immunol. 13, 997786. https://doi.org/10.3389/fimmu.2022.997786.

Viviani, B., Bartesaghi, S., Gardoni, F., Vezzani, A., Behrens, M.M., Bartfai, T., Binaglia, M., Corsini, E., Di Luca, M., Galli, C.L., Marinovich, M., 2003. Interleukin-1beta enhances NMDA receptor-mediated intracellular calcium increase through activation of the src family of kinases. J. Neurosci. Off. J. Soc. Neurosci. 23, 8692–8700. https://doi.org/10.1523/JNEUROSCI.23-25-08692.2003.

Wang, Q., Walsh, D.M., Rowan, M.J., Selkoe, D.J., Anwyl, R., 2004. Block of long-term potentiation by naturally secreted and synthetic amyloid β-Peptide in hippocampal slices is mediated via activation of the kinases c-Jun N-Terminal kinase, cyclin-dependent kinase 5, and p38 mitogen-activated protein kinase as well as metabotropic glutamate receptor type 5. J. Neurosci. 24, 3370–3378. https://doi.org/10.1523/JNEUROSCI.1633-03.2004.

Yan, L., Yin, P., Ma, C., Liu, Y., 2014. Method development and validation for pharmacokinetic and tissue distributions of ellagic acid using ultrahigh performance liquid chromatography-tandem mass spectrometry (UPLC-MS/MS). Molecules 19, 18923–18935. https://doi.org/10.3390/molecules191118923.

Yao, W., Zou, H.-J., Sun, D., Ren, S.-Q., 2013. Aβ induces acute depression of excitatory glutamatergic synaptic transmission through distinct phosphatase-dependent mechanisms in rat CA1 pyramidal neurons. Brain Res. 1515, 88–97. https://doi.org/10.1016/j.brainres.2013.03.049.

Yap, T.E., Balendra, S.I., Almonte, M.T., Cordeiro, M.F., 2019. Retinal correlates of neurological disorders. Ther. Adv. Chronic Dis. 10, 204062231988220. https://doi.org/10.1177/2040622319882205.

Young, K., Morrison, H., 2018. Quantifying microglia morphology from photomicrographs of immunohistochemistry prepared tissue using ImageJ. J. Vis. Exp. 57648. https://doi.org/10.3791/57648.

Zheng, X., Yang, J., Hou, Y., Fang, Y., Wu, K., Song, Y., Liu, K., Zhu, J., 2024. Current non-invasive strategies for brain drug delivery: overcoming blood–brain barrier transport. Mol. Biol. Rep. 51, 25. https://doi.org/10.1007/s11033-023-08968-3.

Zhu, J., Wang, Z., Song, L., Fu, W., Liu, L., 2023. Anti-Alzheimer's natural products derived from plant endophytic fungi. Molecules 28, 2259. https://doi.org/10.3390/molecules28052259.